Title

M2 isoform of pyruvate kinase rewires glucose metabolism during radiation therapy to promote an antioxidant response and glioblastoma radioresistance

Journal

Neuro-Oncology, 25(11)

ISSN

1522-8517

Authors

Bailleul, Justine
Ruan, Yangjingyi
Abdulrahman, Lobna
et al.

Publication Date

2023-11-02

DOI

10.1093/neuonc/noad103

Peer reviewed

Manuscript number: N-O-D-23-00027R1

PKM2 rewires glucose metabolism during radiation therapy to promote an antioxidant response and glioblastoma radioresistance

[1]Justine Bailleul, [1]Yangjingyi Ruan, [1]Lobna Abdulrahman, [7,9]Andrew J. Scott, [1]Taha Yazal, [1]David Sung, [5]Keunseok Park, [1]Hanna Hoang, [1]Juan Nathaniel, [1]Fang-I Chu, [1]Daisy Palomera, [1]Anahita Sehgal, [3]Jonathan E. Tsang, [3]David A. Nathanson, [2,3,4]Shili Xu, [5]Junyoung O. Park, [3]Johanna ten Hoeve, [1]Kruttika Bhat, [8]Nathan Qi, [2,6]Harley I. Kornblum, [1]Dorthe Schaue, [1]William H. McBride, [8,9]Costas A. Lyssiotis, [7,9]Daniel R. Wahl, [1,2]Erina Vlashi*

[1]Department of Radiation Oncology, David Geffen School of Medicine, University of California, Los Angeles, Los Angeles, CA

[2]Jonsson Comprehensive Cancer Center, University of California, Los Angeles, Los Angeles, CA

[3]Department of Molecular and Medical Pharmacology, David Geffen School of Medicine, University of California, Los Angeles, CA

[4]Crump Institute for Molecular Imaging, David Geffen School of Medicine, UCLA, Los Angeles, CA

[5]Department of Chemical and Biomolecular Engineering, University of California, Los Angeles, Los Angeles, CA

[6]Neuropsychiatric Institute–Semel Institute for Neuroscience & Human Behavior, University of California, Los Angeles, CA 90095

[7]Department of Radiation Oncology, University of Michigan, Ann Arbor, MI

[8]Department of Molecular and Integrative Physiology, University of Michigan, Ann Arbor, MI

[9]Rogel Cancer Center, University of Michigan, Ann Arbor, MI

Manuscript number: N-O-D-23-00027R1

Running title: Metabolic rewiring drives glioblastoma radioresistance

*Correspondence should be addressed to EV (e-mail: evlashi@mednet.ucla.edu). Department of Radiation Oncology, David Geffen School of Medicine at UCLA, 10833 Le Conte Ave, Los Angeles, CA 90095-1714, Phone: +1 310 825 3064, Fax: +1 310 206 1260, email: evlashi@mednet.ucla.edu

Funding: Andrew Scott was supported by F32CA260735. Dan Wahl was supported by NCI K08CA234416 (DRW), R37CA258346 (DRW), Cancer Center Support Grant P30CA46592, Damon Runyon Cancer Foundation, Ben and Catherine Ivy Foundation and the Sontag Foundation. David Nathanson and Harley Kornblum were supported by UCLA SPORE in Brain Cancer (P50 CA211015). Erina Vlashi was supported by NCI CA251872 (EV), UCLA SPORE in Brain Cancer (P50 CA211015) (EV), Jonsson Comprehensive Cancer Center at UCLA Seed Grant. The microPET/CT imaging was supported by the Cancer Center Support Grant (2P30CA016042-44).

Conflict of interest: The authors declare no conflict of interest.

Authorship: see Supplementary Material.

Abstract: 218

Text: 3,848

References: 1,009

Figure legends: 890

Manuscript number: N-O-D-23-00027R1

Total: 6,497

ABSTRACT

Background: Resistance to existing therapies is a significant challenge in improving outcomes for glioblastoma (GBM) patients. Metabolic plasticity has emerged as an important contributor to therapy resistance, including radiation therapy (RT). Here, we investigated how GBM cells reprogram their glucose metabolism in response to RT to promote radiation resistance.

Methods: Effects of radiation on glucose metabolism of human GBM specimens were examined *in vitro* and *in vivo* with the use of metabolic and enzymatic assays, targeted metabolomics, and FDG-PET. Radiosensitization potential of interfering with PKM2 activity was tested via gliomasphere formation assays and *in vivo* human GBM models.

Results: Here, we show that RT induces increased glucose utilization by GBM cells, and this is accompanied with translocation of GLUT3 transporters to the cell membrane. Irradiated GBM cells route glucose carbons through the pentose phosphate pathway (PPP) to harness the antioxidant power of the PPP and support survival after radiation. This response is regulated in part by the M2 isoform of pyruvate kinase (PKM2). Activators of PKM2 can antagonize the radiation-induced rewiring of glucose metabolism and radiosensitize GBM cells *in vitro* and *in vivo*.

Conclusions: These findings open the possibility that interventions designed to target cancer-specific regulators of metabolic plasticity, such as PKM2, rather than specific metabolic pathways, have the potential to improve the radiotherapeutic outcomes in GBM patients.

Keywords: Glioblastoma, radiation resistance, metabolism, plasticity, PPP

Key points:

- GBM rewires glucose metabolism to resist oxidative stress induced by radiation
- GLUT3 translocates to the cell surface for more efficient glucose uptake after radiation
- PKM2 regulates glucose flux through the antioxidant PPP following radiation

IMPORTANCE OF THE STUDY

Glioblastomas (GBM) are aggressive brain tumors with dismal prognosis that is in part due to a remarkable resistance to modern therapies, including radiation therapy (RT). This study shows that GBM respond to radiation by rewiring glucose metabolism in a way that promotes survival during RT. Following RT, glioblastomas upregulate glucose consumption by increasing GLUT3 at the cell surface. Glucose-derived metabolites are preferentially routed through the antioxidant PPP, thus optimizing for survival during the lethal oxidative stress induced by radiation. PKM2, is identified as one of the main molecular regulators of the increased flux through the PPP. Small molecule activators of PKM2 show promise for significantly enhancing the therapeutic benefit of RT and improving overall outcomes in this deadly disease.

INTRODUCTION

More than two-thirds of adults diagnosed with glioblastoma (GBM) will die within 2 years of diagnosis, making GBM one of the most lethal of cancers. Post-surgical radiation therapy (RT) combined with temozolomide[1], and more recently the addition of alternating electrical tumor treating fields[2] are currently the only treatment approaches that significantly improve overall

survival, over surgery alone. Yet, GBM tumors inevitably recur, largely within the radiation field[3]. Overcoming radiation resistance of these tumors is one of the major remaining frontiers in radiation oncology that, if resolved, could potentially dramatically improve outcomes in this disease.

Amongst the recognized drivers of the remarkable radioresistance in GBM is tumor metabolism and its potential for promoting resistance to oxidative stress, such as generated during RT. Disparate oncogenic mutations often converge on canonical metabolic pathways that fulfill the enhanced biosynthetic demands during cancer growth, making altered metabolism a recognized hallmark of cancer[4], including GBM[5]. Aerobic glucose catabolism via glycolysis (aerobic glycolysis) is thought to provide an advantage to cancer cells by enhancing the pool of glycolytic intermediates that serve as input for various biosynthetic pathways branching from glycolysis. This partially explains the 'Warburg effect' observed in most tumors[6,7]. Relevant to RT, glycolytic branches, such as the pentose phosphate pathway (PPP) are also critical contributors to the cell's pool of reducing equivalents that maintain a balanced redox status and can thus promote survival under oxidative stress conditions[8].

The last decade brought the recognition that tumors do not have a fixed, albeit aberrant, metabolic profile but rather exhibit remarkable metabolic plasticity that allows for rapid, on-demand reprogramming in an ever-changing tumor microenvironment. We and others have provided evidence for inherent metabolic plasticity in GBM cells[9,10] that presumably provides survival advantages and contributes to therapeutic resistance. The impact of radiation on tumor metabolism, and the molecular regulators involved in metabolic reprogramming during RT remain largely uninvestigated. Here we aim to narrow this knowledge gap as it applies to GBM radiotherapy.

The M2 isoform of pyruvate kinase (PKM2) is a tumor-specific, candidate mediator of GBM metabolic plasticity. PKM2 acts as a 'metabolic switch' to promote rewiring of metabolic fluxes in a context-dependent manner by rapidly shifting between different oligomeric states[11]. Under proliferating conditions, growth factor signaling inhibits the enzymatic activity of PKM2[12]. This creates a bottleneck in glycolysis making upstream glycolytic intermediates available for anabolic pathways, such as the PPP, that support tumor growth. In addition, the PPP contributes to the maintenance of cellular redox balance via the production of NADPH, promoting survival under oxidative stress conditions[13] but the therapeutic implications in RT-resistant cancers remain unknown.

Here, we show that irradiated GBM cells rewire their glucose metabolism to drive a metabolic antioxidant response via the PPP that promotes resistance to the oxidative stress induced by radiation, and that PKM2 is a major regulator of this response. Evidence that PKM2 is overexpressed in GBM tumors, while normal brain tissue expresses the constitutively active PKM1[14,15], points to PKM2 as a potentially actionable therapeutic target for combining with RT. Here, we provide initial evidence that supports this approach.

MATERIALS AND METHODS

Cell culture: Primary human glioblastoma lines, GBM217, GBM374, GBM382 were established at UCLA as described in Laks *et al.*[16]. Patient-derived xenografts (GBM38)[17] were provided by Dr. Jann Sarkaria (Mayo Clinic). See Supplementary Materials and Methods (M&M) for more details.

Irradiation and treatments: Cells were irradiated at room temperature using an experimental X-ray irradiator (Gulmay Medical Inc, Suwanee, GA) at a dose rate of 7.1702 Gy/min. Unless otherwise stated, cells were treated with 10 μM of the PKM2 activator, TEPP46 (MedChem Express) 3 hours prior to irradiation. 2-Deoxy-D-Glucose, 2DG (Sigma) was used at a dose of 5 mM in glucose-free complete GBM media, 2 hours prior to irradiation. GSH-MEE (Sigma) was used at 5 mM, 5 minutes prior to irradiation. See Supplementary M&M for more details.

Gliomasphere formation assay: Gliomasphere-forming capacity was determined by plating cells in GBM media, into 96-well non-treated plates, at a range of cell densities appropriate for the different cell lines and doses of radiation. The surviving fraction was determined as previously described[18]. See Supplementary M&M for more details.

Glucose uptake, lactate production and ROS detection: see Supplementary M&M.

G6PDH, 6PGD and PKM2 activity assays: see Supplementary M&M.

***In vitro* Metabolomics:** For metabolite extraction and measurement methods See Supplementary M&M.

Immunofluorescence and Immunocytochemistry: see Supplementary M&M.

Protein extraction, cell fractionation, western blotting, RNA extraction and real-time quantitative polymerase chain reaction (RT qPCR): see Supplementary M&M.

Subcutaneous tumor models in mice: GBM374 cells were suspended in a solution of 1:1 mixture of Matrigel® basement membrane matrix (Corning) and DMEM medium and 50,000 cells were injected subcutaneously in the hind legs of NSG. For details on treatments see Supplementary M&M.

Intracranial tumor models

Survival studies: GBM cells were implanted into the right striatum of the brains of mice using a stereotactic device. For more details on implantation methods, treatments and IHC staining of brain tissue see Supplementary M&M.

In vivo **stable isotope tracing:** For details see Supplementary M&M.

In vivo **micro-PET/micro-computed tomography (CT) imaging:** Male NSG mice were implanted subcutaneously with GBM374 gliomaspheres. Once the tumors were palpable, mice underwent micro-PET imaging immediately followed by microCT imaging in the Genisys8 scanner (Sofie Biosciences). For details see Supplementary M&M.

Brain penetration of PKM2-activator: For sample preparation and detection see Supplementary M&M.

Statistics: Unless otherwise stated, statistical significance was determined by performing two-sided t tests or two-way ANOVA using Prism v9.3.0. *p* values were considered significant below

0.05 (*, $p<0.05$; **, $p<0.01$, ***, $p<0.001$, ****, $p<0.0001$). All experiments were independently repeated at least 3 times.

See Supplementary M&M for statistical analysis of *Subcutaneous tumor model and Intracranial model.*

Data availability: Raw data for the metabolomics study were generated at the UCLA Metabolomics center and at the University of Michigan Metabolomics core. Derived data supporting the findings of this study are available from the corresponding author upon request. Other data generated in this study are presented within the article and its supplementary files.

Ethics: For *in vivo* experiments, all animal procedures were approved by the UCLA Institutional Animal Care and Use Committee and by the University Committee on Use and Care of Animals at the University of Michigan.

RESULTS

1. Radiation induces an enhanced "Warburg-like" metabolic phenotype in GBM

To determine the effect of radiation on glucose utilization, we used patient-derived, treatment-naïve GBM specimens with defined genetic features and mutation status (see Materials and Methods), that were propagated as gliomaspheres (gs) shown to maintain the phenotype of originating tumors[19]. The fluorescent analogue of glucose, 2NBDG was used as a surrogate for "glucose uptake". The *in vitro* basal glucose uptake (Supplementary Fig. 1A) reflected the relative growth rates of the different gliomasphere specimens (Supplementary Fig. 1B-C). Adherent (ad)

cultures, established by growing gliomaspheres in the presence of serum, took up more 2NBDG relative to gliomaspheres (Supplementary Fig. 1D). All cultures significantly increased 2NBDG uptake following radiation by as much as 2-fold, in a radiation dose-dependent manner (Fig. 1A-C, Supplementary Fig. 1E-F), despite the expected slower growth rate (Supplementary Fig. 1G) and smaller spheroid sizes of irradiated gliomaspheres (see Fig. 3F). To determine if the enhanced glucose uptake persists beyond the first 72 hours following radiation, we measured 2NBDG uptake in sequential generations of gliomaspheres (Supplementary Fig. 1H). Glucose uptake remained elevated for up to two weeks following the initial radiation exposure with a single dose of 8 Gy (Fig. 1D and Supplementary Fig. 1I).

To validate the observations obtained with the 2NBDG method, we used biochemistry analyzers (YSI) as a complementary method that allows for a more direct, time-resolved, per cell basis measure of extracellular glucose concentration in growth media without disturbance to cell growth. This method confirmed the enhanced uptake of glucose by gliomaspheres with similar time kinetics following radiation (Fig. 1E-F).

In general, cancer cells, including GBMs, convert most of the glucose carbons to lactate via glycolysis, even when oxygen is readily available (Warburg effect[6]). Similarly, irradiated gliomaspheres secrete more lactate (Fig. 1G), suggesting that at least some of the 'extra' glucose taken up following radiation is being converted to lactate.

To determine whether the enhanced glucose utilization following radiation also occurs *in vivo,* we used the glucose analogue [^{18}F]fluorodeoxyglucose ([^{18}F]-FDG), which allows for imaging of glucose uptake *in vivo* via PET. Consistent with the *in vitro* observations, subcutaneous GBM

tumors took up significantly more glucose at 24 hours and 5 days following radiation (Fig. 1H-I, Supplementary Fig. 1J-K).

2. Radiation induces translocation of glucose transporter 3 (GLUT3) to the cell membrane

To probe the mechanism behind the increase in glucose uptake by irradiated gliomaspheres we analyzed levels of the main glucose transporters (GLUT) and hexokinases (HK) in GBM cells (Fig. 2A). Only HK2 gene expression levels increased following radiation (Fig. 2A). At the protein level, GLUT1 levels were extremely low compared to GLUT3 and did not change following radiation (Supplementary Fig. 2A). While GLUT3 was abundant (Supplementary Fig. 2A) its total protein levels decreased following radiation (Fig. 2B), reflecting the decreased gene expression levels (Fig. 2A). Although gene expression levels of HK2, the predominant isoform in GBM, increased following radiation (Fig. 2A), this did not correlate with increased protein levels (Fig. 2C, Supplementary Fig. 2B). Therefore, total protein levels of GLUTs or HKs did not explain the increase in glucose uptake following radiation.

We then explored the possibility that glucose transporters translocate to the cell membrane more efficiently following radiation, thus providing irradiated GBM cells with a greater capacity to take up glucose. Immunofluorescence analysis revealed increased levels of GLUT3 on the cell surface following radiation, in both gliomaspheres (Fig. 2D) and adherent cultures (Supplementary Fig. 2C), whereas GLUT1 cell surface levels remained relatively similar (Supplementary Fig. 2D). The radiation-induced increase in cell surface levels of GLUT3 was also confirmed via cell fractionation methods (Fig. 2E-F) and quantitatively via flow cytometry (Fig. 2G-I) and closely mirrored the kinetics of glucose uptake by gliomaspheres (Fig. 2G-I, right hand panels). The fold-change in 2NBDG uptake induced by radiation linearly correlated with the fold-change in cell

surface levels of GLUT3 (Fig. 2J), providing a plausible explanation for the increase in glucose uptake by irradiated gliomaspheres (Fig. 1).

3. Radiation rewires glucose metabolism to enhance PPP activity

We hypothesized that the increase in glucose uptake by irradiated gliomaspheres is a response to the oxidative stress induced by radiation. To test this, we irradiated gliomaspheres in the presence of a potent antioxidant, reduced glutathione (GSH), provided in the form of glutathione reduced ethyl ester (GSH-MEE), a membrane/lipid permeable derivative of GSH, at concentrations that prevent the accumulation of radiation-induced reactive oxygen species (ROS) (Fig. 3A, Supplementary Fig. 3A). GSH partially or fully prevented the increase in glucose uptake (Fig. 3B), pointing to an adaptive role for glucose in mitigating the oxidative stress induced by radiation.

To understand the fate of glucose carbons in irradiated gliomaspheres, we measured metabolite levels via LC-MS using untargeted and targeted metabolomics. Untargeted analysis revealed that total abundance levels of glucose and metabolites in upper glycolysis, such as phosphorylated glucose/fructose-6-phosphate (G6P/F6P), fructose-1,6-bisphosphate (F1,6BP) and 3-phosphoglycerate (3PG) increased following radiation (Fig. 3C and Supplementary Fig. 3B-C). G6P serves as the branching point of glycolysis into the oxidative (ox) arm of the PPP (oxPPP), while F6P, F1,6BP and 3PG can reversibly feed into the non-oxidative (non-ox) PPP arm (Fig. 3D). Analysis of abundance levels of PPP metabolites, such as 6-phosphogluconate (6PG) and ribulose-5-phosphate (R5P) in the oxPPP, and sedoheptulose 7-phosphate (S7P) in the non-oxPPP revealed increased abundance in irradiated gliomaspheres (Fig. 3C and Supplementary Fig. 3B-C).

Abundance of metabolite levels is the net result of metabolite production and consumption and does not inform on metabolic flux. Therefore, to better understand the flux of glucose carbons following radiation, we performed 1,2-$^{13}C_2$-glucose tracing experiments and analyzed the ^{13}C-labeled metabolite levels via LC-MS to distinguish glucose carbons routed through the PPP from those oxidized strictly via glycolysis[20] (Fig. 3D-E). As depicted in Fig. 3D, HK converts 1,2-$^{13}C_2$-glucose to 1,2-$^{13}C_2$-G6P, which can either be metabolized through glycolysis or through the PPP. When metabolized through glycolysis, the downstream metabolites will maintain two ^{13}C-labeled carbons (M+2). When 1,2-$^{13}C_2$-G6P is shunted through the PPP, an oxidative decarboxylation reaction removes the ^{13}C label on the first position of glucose, generating singly ^{13}C-labeled metabolites (M+1), some of which feed back into the glycolysis pathway via the non-oxPPP (Fig. 3D). We used the difference in lactate ^{13}C-labeling (Supplementary Fig. 3D-E) normalized by the rate of glucose consumption (as determined in Fig. 1E-F) to calculate absolute flux of glucose carbons through the PPP. Despite the heterogeneity in sphere sizes and growth rates (Fig. 3E-F), targeted metabolomics analysis revealed a clear increase in PPP flux in irradiated gliomaspheres that becomes significant by 24 hours following radiation and is sustained for up to at least 72 hours, the last time point analyzed (Fig. 3G-H).

The 1,2-$^{13}C_2$-glucose tracer is less adequate for determining PPP flux *in vivo* due to label mixing in other tissues and the circulatory system that would produce many different, unexpected forms of labeled glucose. Therefore, we used a uniformly labeled ^{13}C-glucose tracer to infuse a mouse intracranial model of patient-derived gliomaspheres (Fig. 3I). We observed that the G6P-derived fraction of R5P was increased in irradiated tumors, indicative of enhanced PPP activity (Fig. 3I and Supplementary Fig. 3F).

4. PKM2 enables the radiation-induced increase in PPP activity to harness its antioxidant power

The enzymatic activity of the first rate-limiting enzyme in the PPP, glucose-6-phosphate dehydrogenase (G6PDH), or the second enzyme, 6-phosphogluconate dehydrogenase (6PGD) were not affected by radiation, although oxidative stress induced by hydrogen peroxide (H_2O_2) significantly downregulates G6PDH activity (Supplementary Fig. 4A-B). This indicated that the radiation-induced shunting of glucose carbons through the PPP (Fig. 3G-H) cannot be explained by alterations in PPP enzyme activity. Others have shown that acute oxidative stress induced via means other than radiation, inhibits the enzymatic activity of the last rate-limiting enzyme in glycolysis, PKM2 and that this supports antioxidant production by promoting glucose oxidation via the PPP[13]. Since the increase in glucose uptake by irradiated gliomaspheres (Fig. 1) is accompanied by increased PPP flux (Fig. 3G-I) and this seems to be a response to oxidative stress generated by radiation (Fig. 3B), we considered the possibility that oxidative stress induced by radiation inhibits PKM2 activity, resulting in increased PPP flux.

Although radiation had no effect on PKM2 protein levels (Supplementary Fig. 4C-E) it suppressed its enzymatic activity (Fig. 4A), but this was prevented by the addition of GSH-MEE (Fig. 4B and Supplementary Fig. 4F), suggesting that radiation-induced oxidative stress promotes the suppression of PKM2 activity. The addition of the reducing agent dithiothreitol (DTT) to the cell lysate prior to measuring PK activity, partially restored PKM2 activity (Fig. 4B and Supplementary Fig. 4F), pointing to a reversible oxidizing event as the likely culprit for the suppressed PKM2 activity. TEPP46, a small molecule activator of PKM2[21] (Supplementary Fig. 4G-H) prevented the suppression of PKM2 activity (Fig. 4C) and the increase in lactate secretion following radiation

(Fig. 4D). Although TEPP46 had no effect on basal PPP flux, it dampened the radiation-induced increase (Fig. 4E), pointing to PKM2 as a promoter of enhanced PPP flux following radiation of gliomaspheres.

The increase in PPP flux is accompanied by increased NADPH and GSH abundance levels (Supplementary Fig. 4I-J), suggesting a PPP contribution to the NADPH/GSH pool following radiation. While PKM2 activators do not seem to affect NADPH levels (Fig. 4F-G), pointing to other sources of NADPH production following radiation, they do reduce GSH levels (Fig. 4H-I). This suggests that radiation-induced ROS levels should be exacerbated when PKM2 is activated. Indeed, TEPP46 increases ROS levels following radiation (Fig. 4J-K). Alternatively, NADPH supply via the PPP can be increased by providing cells with 2-deoxyglucose (2DG). Although 2DG is a commonly used glycolysis inhibitor that cannot be shunted into the glycolysis pathway downstream of phosphoglucose isomerase, it can still be shunted into the PPP to produce NADPH[22,23]. 2DG dampened ROS accumulation in irradiated gliomaspheres (Fig. 4J-K), likely by stimulating NADPH production via the PPP and maintaining reduced GSH pools. Analysis of PKM2 expression levels in the TCGA glioblastoma cohort revealed a strong correlation to progression-free survival (Fig. 4L), highlighting an important role for PKM2 in GBM and suggesting that PKM2 might be a potential therapeutic target.

5. PKM2 activators sensitize GBM to radiation therapy

We evaluated the potential of pharmacological activation of PKM2 via TEPP46 in radiosensitizing GBM. Using a modified *in vitro* clonogenic 'sphere forming assays' (SFA, See Materials and Methods) we showed that TEPP46 radiosensitizes gliomaspheres from all three lines (Fig. 5A-C)

and this effect lasts beyond the first generation of gliomaspheres (Fig. 5D). Relevant to potential *in vivo* application, TEPP46 had no apparent effect as a single agent or as a radiosensitizer on normal human astrocytes *in vitro* (Fig. 5E), indicating that PKM2 activators will not affect normal brain cells, which likely rely more on PKM1 for their metabolic needs[14].

In vivo, we determined the effect of combining TEPP46 with radiation in subcutaneous (sub-c) and orthotopic xenograft models of human GBM. In the 374gs sub-c model, TEPP46 alone was initially more efficient at controlling tumor growth than fractionated radiation (Fig. 6A). However, combining TEPP46 with radiation resulted in sustained tumor control over time and in some cases, tumor regression (Fig. 6A and Supplementary Fig. 5A-B). Linear mixed-effects modeling identified significant negative effects of the combination regimen on tumor growth rate (Supplementary Fig. 5C-D). The tumor average maximum growth rates, as estimated by smoothing spline for vehicle, radiation, TEPP46 or combined treatment were 0.18, 0.14, 0.17 and 0.07, respectively. TEPP46 had no apparent effect on the weights of the mice, supporting a favorable overall toxicity profile (Supplementary Fig. 5E).

Previous studies show that TEPP46 penetrates the blood brain barrier[24], therefore we evaluated the therapeutic potential of TEPP46 in orthotopic GBM models with different median survival times: 217gs, median survival ~3 weeks and 374gs, median survival ~5 weeks. Our own evaluation of the *in vivo* pharmacokinetics of TEPP46 administered intraperitoneally showed that the brain-to-plasma area under the curve (AUC, 0-24 hours) for TEPP46 in non-tumor bearing mice is ~13%, with a plasma and brain half-life of around 4 hours (Fig. 6B). As a single agent, TEPP46 had no impact on the overall survival for either model however, the combination treatment had a significant radiosensitizing effect, but only at the higher dose of 50 mg/kg of TEPP46 (Fig. 6C-D). This combination treatment resulted in the greatest estimated median survival of 33 and 56

days for GBM217 and GBM374 respectively, and the lowest hazard ratio among all the groups, with 8 Gy as the reference group (Fig. 6C-D, Supplementary Fig. 5F-G). Notably, we observed long-term survivors with no detectable tumors in both TEPP46 doses in the GBM374 model (Fig. 6E, Supplementary Fig. 5H). These results suggest that the lower dosing of TEPP46 might not be reaching therapeutic concentrations in the brain. Despite this apparent limitation of TEPP46 availability *in vivo*, three out of eight mice survived tumor-free for over 3 months, in the slower-growing GBM374 model (Fig. 6C and E and Supplementary Fig. 5H-I).

DISCUSSION

The reconfiguration of carbohydrate metabolism as a regulated response to cellular oxidative stress has been recognized for over two decades, including the oxidative stress-induced rerouting of glucose carbons into the oxPPP[25,26]. Here, we report that GBM cells retain a remarkable degree of metabolic plasticity that supports their survival during oxidative stress induced by RT. They consume additional glucose following irradiation (Fig. 1), akin to our observations in breast cancer[27]. Early studies have reported similar observations of a rapid rise in glucose uptake during RT, via [^{18}F]-FDG-PET imaging of mouse and human tumors[28,29], pointing to a more general response of tumors treated with RT. Antioxidants prevent the increase in glucose uptake (Fig. 3A-B), pointing to the radiation-induced oxidative stress as the likely 'signal' for this response, in line with reports of a ROS-dependent increase in tumor glucose demand following radiation of mammary carcinomas[30].

Our findings show that radiation promotes a net outward translocation of GLUT3 to the cell's surface accounting for the changes in glucose transport following radiation (Fig. 6F). Although the mechanism of radiation-induced translocation of GLUT3 remains to be determined, the

involvement of GLUT3 in facilitating increased glucose consumption by irradiated GBM cells is not surprising. GLUT3 has a higher affinity for glucose than GLUT1, 2 or 4 and ~fivefold greater transport capacity than GLUT1 or 4[31], ensuring efficient glucose uptake. GLUT3 is critical to the survival of GBM stem cells in low glucose[32] and subpopulations of GBM are GLUT3-addicted[33]. While GLUT1 and GLUT3 are the two main transporters in cerebral glucose metabolism, only GLUT3 levels predict for poor GBM survival[32,33].

Our findings show that the radiation-induced increase in PPP flux is regulated, in part, by the suppression of PKM2 activity in gliomaspheres, due to an oxidative event (Fig. 4A-B). Oxidized, kinase-*inactive* PKM2 blocks pyruvate production, making upstream glycolytic intermediates available for the PPP, one of the main sources of cellular NADPH[13]. PKM2 activators reduce flux of glucose carbons through the PPP (Fig. 4E), exacerbates ROS levels (Fig. 4J-K) and radiosensitize GBM (Fig. 5-6). Together, these findings posit that enhanced carbon flux through the PPP is a PKM2-regulated, pro-survival metabolic response in irradiated GBM (Fig. 6F). Although not investigated here, another potential benefit from enhanced PPP flux is the generation of nucleotide precursors for DNA repair[34], a possibility that warrants further investigation.

Although seemingly contradictory, our findings are in line with others showing radiosensitization of GBM cells by knocking down PKM2 expression[35,36]. PKM2 can readily switch between an enzymatically *active-tetramer* and an *inactive-dimer*, altering glycolytic flux. The dimers can also translocate to the nucleus where they moonlight as regulators of DNA repair, as is demonstrated by the Sizemore and Wu studies[35,36]. Knocking down PKM2 would abrogate both the *dimeric* and *tetrameric* forms of PKM2, therefore abrogating both of its functions as a regulator of glycolytic flux in the cytosol and a regulator of DNA repair in the nucleus, whereas our approach is to alter

the balance between the two conformations using the small molecule activator TEPP46, that could have greater clinical relevance.

Clearly, normal cells are also capable of reconfiguring glycolytic flux as a way to mitigate oxidative stress[22,25,26] and redox-sensitive metabolic enzymes, such as GAPDH can regulate this response in normal cells[37]. Therefore, identifying cancer-specific regulators of redox metabolic plasticity for therapeutic targeting is crucial to the success of this approach. PKM2 is overexpressed in GBM[15,24], making it an attractive target of 'metabolic plasticity' for GBM radiosensitization. Small molecule activators of PKM2 show promise in slowing tumor growth in xenograft models[21,38] prompting clinical trial testing as single agents (Clinicaltrials.gov, NCT04328740, recruiting), yet to be combined with other anti-cancer therapies, including RT. The development of PKM2 imaging agents in brain tumors[15,39,40], provides an additional opportunity for coupling treatment with target imaging to optimize potential for benefit. Despite critical differences, many parallels exist between the metabolic regulation of rapidly proliferating cancer cells and activated immune effector cells[41]. Evidence exists, although none in tumor models, suggesting that activation of PKM2 hampers immune cell activation[42,43]. Therefore, PKM2 targeting needs further validation in the context of an intact immune system to fully support its radiotherapeutic potential.

ADDITIONAL INFORMATION

Acknowledgments:

We thank Min Li and Mansoureh Eghbali, Department of Anesthesiology at UCLA, for their support in acquiring confocal images. We thank Mikayla Tamboline for her help with the microPET/CT imaging experiments in the UCLA Crump Preclinical Imaging Technology Center.

REFERENCES

1. Stupp, R.*, et al.* Radiotherapy plus concomitant and adjuvant temozolomide for glioblastoma. *The New England journal of medicine* **352**, 987-996 (2005).
2. Fabian, D.*, et al.* Treatment of Glioblastoma (GBM) with the Addition of Tumor-Treating Fields (TTF): A Review. *Cancers* **11**(2019).
3. Chamberlain, M.C. Radiographic patterns of relapse in glioblastoma. *Journal of neuro-oncology* **101**, 319-323 (2011).
4. Pavlova, N.N. & Thompson, C.B. The Emerging Hallmarks of Cancer Metabolism. *Cell metabolism* **23**, 27-47 (2016).
5. Zhou, W. & Wahl, D.R. Metabolic Abnormalities in Glioblastoma and Metabolic Strategies to Overcome Treatment Resistance. *Cancers* **11**(2019).
6. Warburg, O. On the metabolism of carcinoma cells. *Biochem Z.* **152**, 309 (1924).
7. DeBerardinis, R.J. & Chandel, N.S. We need to talk about the Warburg effect. *Nat Metab* **2**, 127-129 (2020).
8. Moreira, J.D.*, et al.* The Redox Status of Cancer Cells Supports Mechanisms behind the Warburg Effect. *Metabolites* **6**(2016).

9. Vlashi, E.*, et al.* Metabolic state of glioma stem cells and nontumorigenic cells. *Proceedings of the National Academy of Sciences of the United States of America* **108**, 16062-16067 (2011).

10. Shibao, S.*, et al.* Metabolic heterogeneity and plasticity of glioma stem cells in a mouse glioblastoma model. *Neuro-oncology* **20**, 343-354 (2018).

11. Chaneton, B. & Gottlieb, E. Rocking cell metabolism: revised functions of the key glycolytic regulator PKM2 in cancer. *Trends in biochemical sciences* **37**, 309-316 (2012).

12. Christofk, H.R.*, et al.* The M2 splice isoform of pyruvate kinase is important for cancer metabolism and tumour growth. *Nature* **452**, 230-233 (2008).

13. Anastasiou, D.*, et al.* Inhibition of pyruvate kinase M2 by reactive oxygen species contributes to cellular antioxidant responses. *Science (New York, N.Y.)* **334**, 1278-1283 (2011).

14. Mukherjee, J.*, et al.* Pyruvate kinase M2 expression, but not pyruvate kinase activity, is up-regulated in a grade-specific manner in human glioma. *PloS one* **8**, e57610 (2013).

15. Beinat, C.*, et al.* A Clinical PET Imaging Tracer ([(18)F]DASA-23) to Monitor Pyruvate Kinase M2 Induced Glycolytic Reprogramming in Glioblastoma. *Clinical cancer research : an official journal of the American Association for Cancer Research* (2021).

16. Laks, D.R.*, et al.* Large-scale assessment of the gliomasphere model system. *Neuro-oncology* **18**, 1367-1378 (2016).

17. Zhou, W.*, et al.* Purine metabolism regulates DNA repair and therapy resistance in glioblastoma. *Nature communications* **11**, 3811 (2020).

18. Yazal, T.*, et al.* Radiosensitizing Pancreatic Cancer via Effective Autophagy Inhibition. *Molecular cancer therapeutics* (2021).

19. Gosa, L., Ta, L. & Nathanson, D.A. Processing of Primary Patient Tumors and Subsequent Generation of Primary Cell Lines. *Methods in molecular biology (Clifton, N.J.)* **1897**, 425-431 (2019).

20. Lee, W.N.*, et al.* Mass isotopomer study of the nonoxidative pathways of the pentose cycle with [1,2-13C2]glucose. *Am J Physiol* **274**, E843-851 (1998).

21. Anastasiou, D.*, et al.* Pyruvate kinase M2 activators promote tetramer formation and suppress tumorigenesis. *Nature chemical biology* **8**, 839-847 (2012).

22. Le Goffe, C.*, et al.* Metabolic control of resistance of human epithelial cells to H2O2 and NO stresses. *The Biochemical journal* **364**, 349-359 (2002).

23. Liu, X.*, et al.* Cystine transporter regulation of pentose phosphate pathway dependency and disulfide stress exposes a targetable metabolic vulnerability in cancer. *Nature cell biology* **22**, 476-486 (2020).

24. Witney TH, J.M., Shen B, Chang E, Pohling C, Arksey N, Hoehne A, Shuhendler A, Park JH, Bodapati D, Weber J, Gowrishankar G, Rao J, Chin FT, Gamhir SS. PET imaging of tumor glycolysis downstream of hexokinase through noninvasive measurement of pyruvate kinase M2. *Science Translational Medicine* **7**, 310 (2015).

25. Grant, C.M. Metabolic reconfiguration is a regulated response to oxidative stress. *Journal of biology* **7**, 1 (2008).

26. Ralser, M.*, et al.* Dynamic rerouting of the carbohydrate flux is key to counteracting oxidative stress. *Journal of biology* **6**, 10 (2007).

27. Zhang, L.*, et al.* PK-M2-mediated metabolic changes in breast cancer cells induced by ionizing radiation. *Breast cancer research and treatment* **178**, 75-86 (2019).

28. Furuta, M.*, et al.* Rapid rise in FDG uptake in an irradiated human tumour xenograft. *Eur J Nucl Med* **24**, 435-438 (1997).

29. Hautzel, H. & Muller-Gartner, H.W. Early changes in fluorine-18-FDG uptake during radiotherapy. *J Nucl Med* **38**, 1384-1386 (1997).

30. Zhong, J.*, et al.* Radiation induces aerobic glycolysis through reactive oxygen species. *Radiotherapy and oncology : journal of the European Society for Therapeutic Radiology and Oncology* **106**, 390-396 (2013).

31. Simpson, I.A.*, et al.* The facilitative glucose transporter GLUT3: 20 years of distinction. *Am J Physiol Endocrinol Metab* **295**, E242-253 (2008).

32. Flavahan, W.A.*, et al.* Brain tumor initiating cells adapt to restricted nutrition through preferential glucose uptake. *Nature neuroscience* **16**, 1373-1382 (2013).

33. Cosset, E.*, et al.* Glut3 Addiction Is a Druggable Vulnerability for a Molecularly Defined Subpopulation of Glioblastoma. *Cancer cell* **32**, 856-868 e855 (2017).

34. Tong, X., Zhao, F. & Thompson, C.B. The molecular determinants of de novo nucleotide biosynthesis in cancer cells. *Curr Opin Genet Dev* **19**, 32-37 (2009).

35. Wu, S.*, et al.* Pyruvate Facilitates FACT-Mediated γH2AX Loading to Chromatin and Promotes the Radiation Resistance of Glioblastoma. *Adv Sci (Weinh)* **9**, e2104055 (2022).

36. Sizemore, S.T.*, et al.* Pyruvate kinase M2 regulates homologous recombination-mediated DNA double-strand break repair. *Cell research* (2018).

37. Kuehne, A.*, et al.* Acute Activation of Oxidative Pentose Phosphate Pathway as First-Line Response to Oxidative Stress in Human Skin Cells. *Molecular cell* **59**, 359-371 (2015).

38. Parnell, K.M.*, et al.* Pharmacologic activation of PKM2 slows lung tumor xenograft growth. *Molecular cancer therapeutics* **12**, 1453-1460 (2013).

39. Beinat, C.*, et al.* Human biodistribution and radiation dosimetry of [(18)F]DASA-23, a PET probe targeting pyruvate kinase M2. *Eur J Nucl Med Mol Imaging* (2020).

40. Wang, D.*, et al.* TEPP-46-Based AIE Fluorescent Probe for Detection and Bioimaging of PKM2 in Living Cells. *Anal Chem* (2021).

41. Andrejeva, G. & Rathmell, J.C. Similarities and Distinctions of Cancer and Immune Metabolism in Inflammation and Tumors. *Cell metabolism* **26**, 49-70 (2017).

42. Palsson-McDermott, E.M.*, et al.* Pyruvate Kinase M2 Regulates Hif-1alpha Activity and IL-1beta Induction and Is a Critical Determinant of the Warburg Effect in LPS-Activated Macrophages. *Cell metabolism* **21**, 347 (2015).

43. Kono, M.*, et al.* Pyruvate kinase M2 is requisite for Th1 and Th17 differentiation. *JCI insight* **4**(2019).

Figure 1.

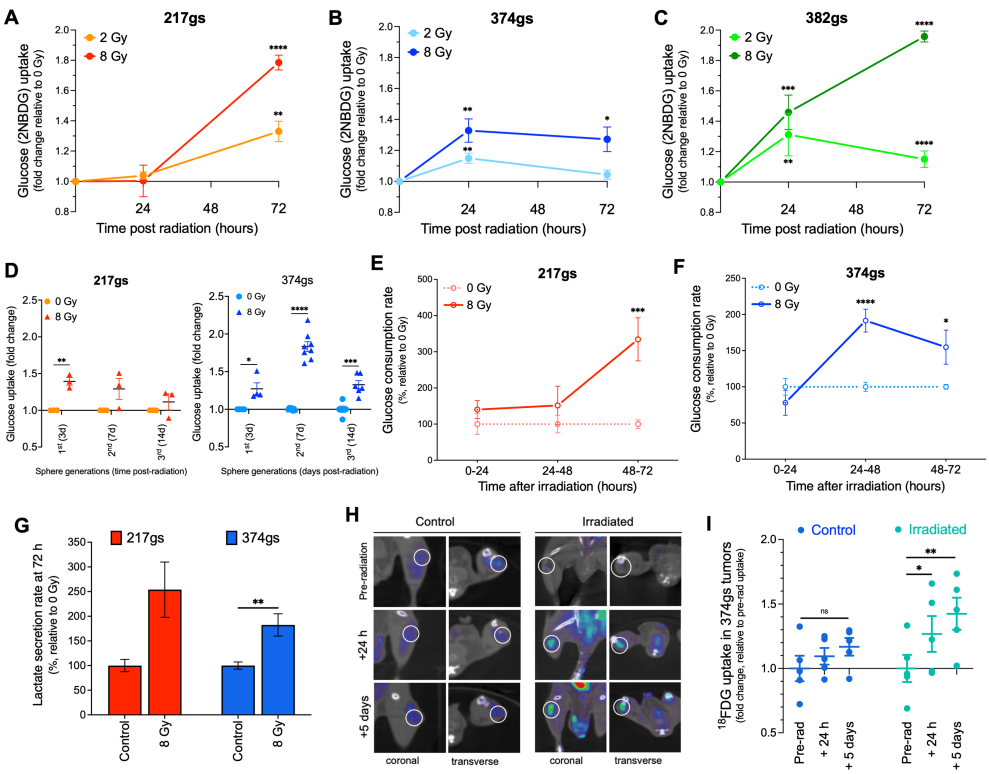

Figure 1. Radiation increases glucose consumption in GBM. (**A-D**) Glucose uptake measured via flow cytometry (2NBDG assay) in GBM217 (**A**), GBM374 (**B**) and GBM382 (**C**) gliomaspheres (gs). Unpaired *t*-tests, n=3. (**D**) Glucose uptake after sequential generations of GBM217gs and GBM374gs following radiation. Unpaired *t*-tests, n=3-4. (**E-F**) Glucose consumption rate determined via YSI biochemistry analyzer, in GBM217gs (**E**) and GBM374gs (**F**). Paired *t*-tests, n=3. (**G**) Lactate secretion rate per cell determined via YSI. Paired *t*-tests, n=3. (**H-I**) Glucose uptake measured via PET scan in tumor-bearing mice infused i.v. with ^{18}F-FDG. Tumors outlined with a white circle on representative images (**H**). FDG uptake levels. Paired *t*-tests, n=4 (**I**).

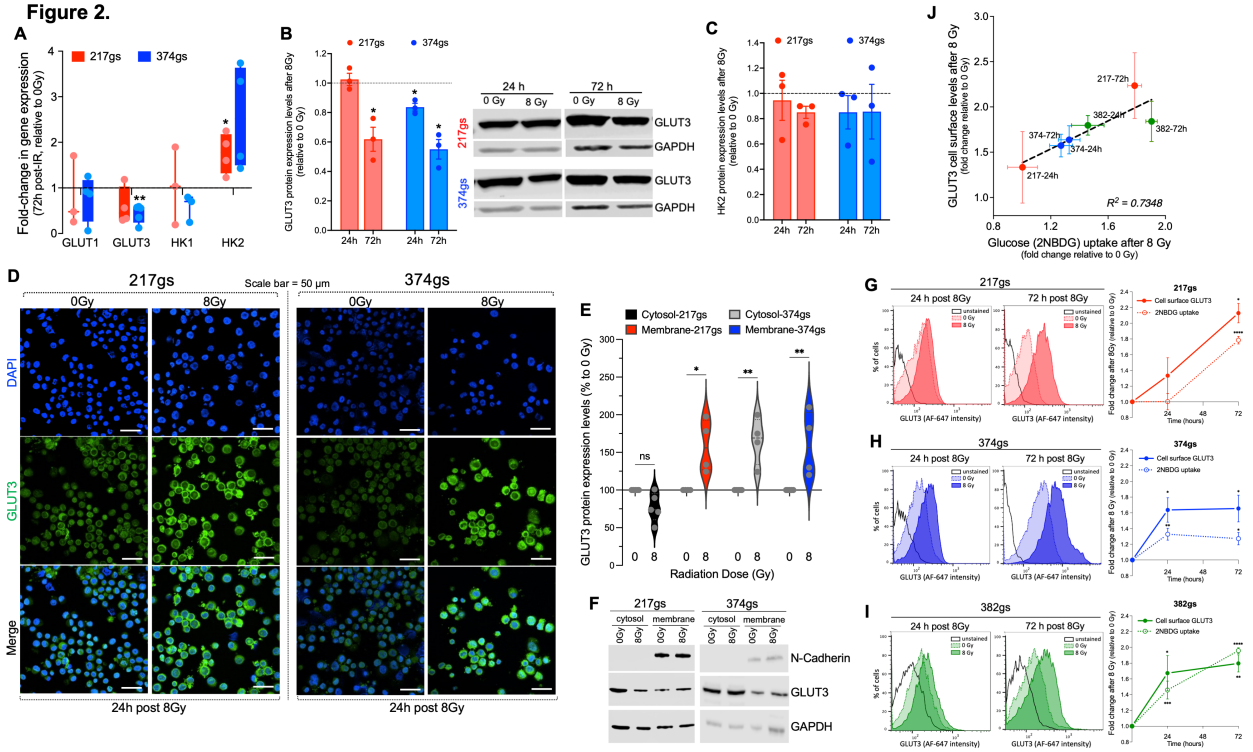

Figure 2. Radiation induces translocation of glucose transporters to the cell membrane. (**A**) GLUT1/3 and HK1/2 gene expression levels. Unpaired *t*-tests, n=3. (**B**) GLUT3 total protein levels. Unpaired *t*-tests, n=3. (**C**) HK2 total protein levels. Unpaired *t*-tests, n=3. (**D**) Cell surface GLUT3 protein levels via confocal microscopy at 40x. Scale bar = 50 µm. (**E-F**) Cytosolic and membrane levels of GLUT3 protein at 24 h post-radiation. Two-way ANOVA, n=3. (**G-I**) Cell surface GLUT3 protein levels via flow cytometry (left histogram panels) quantified and overlayed with 2NBDG uptake levels from Fig. 1A-C (right panels). Unpaired *t*-tests, n=3. (**J**) Correlation between fold change in GLUT3 protein levels at the cell surface and fold change in glucose uptake.

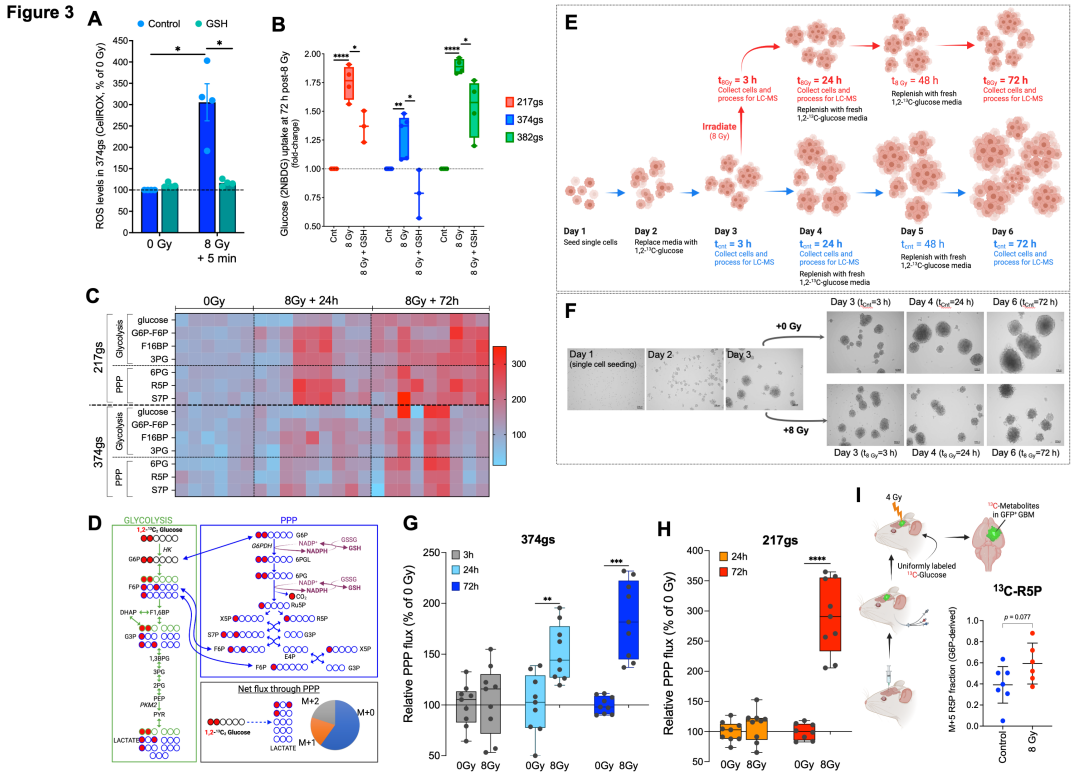

Figure 3. Irradiated gliomaspheres enhance flux through the PPP. (**A**) ROS levels determined with CellROX 5 min after radiation. Unpaired *t*-tests, n=4. (**B**) Glucose uptake via 2NBDG, with 5 mM GSH added prior to radiation. Unpaired *t*-tests, n=4. (**C**) Heatmap of relative ion counts for glycolytic and PPP metabolite levels. Pyruvate levels were not detectable. (**D**) 1,2-$^{13}C_2$ glucose flux and labeled carbon distribution through glycolysis (in green) and the PPP (in blue). Net flux through the PPP results in three M+0 lactates, one M+1 lactate and one M+2 lactate. (**E**) Protocol for glucose flux measurement. (**F**) Images of GBM374gs growth (10x). (**G-H**) Relative PPP flux was determined via glucose tracing experiments, using M+1 and M+2 lactate levels and glucose uptake rates in GBM217gs and GBM374gs treated as depicted in Fig. 3E. Two-way ANOVA, n=3. (**I**) Tissues were harvested from patient-derived GBM38 intracranial tumors, then assessed for ^{13}C labeling by LC-MS. Fractions of ribose 5-phosphate (R5P) produced directly from the

oxidative arm of the PPP were determined by dividing the M+5 fraction of R5P by the M+6 fraction of G6P. Unpaired *t*-tests, n=6-7.

Figure 4

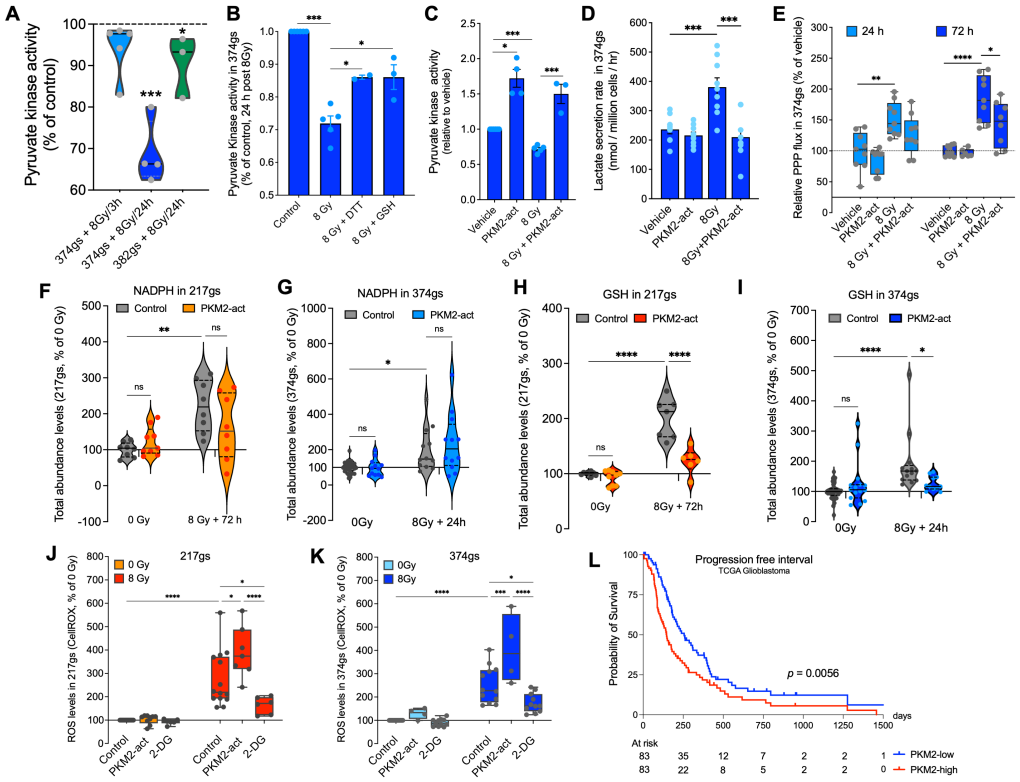

Figure 4. Radiation suppresses PKM2 enzymatic activity, which regulates glucose flux through the PPP. (**A**) Violin plots of PK activity in GBM374gs and GBM382gs after radiation. Dotted line represents the 0 Gy control. (**B-C**) PK activity in the presence of DTT (1 mM) or GSH (5 mM) added prior to radiation (**B**) or in the presence of a PKM2 activator (TEPP46) (**C**). Unpaired *t*-tests, n=3. (**D**) Lactate secretion per cell via YSI in GBM374gs, 72 h post-radiation. Paired *t*-tests, n=3. (**E**) Relative PPP flux determined from M+1 and M+2 lactate levels and glucose uptake rates in GBM374gs. Unpaired *t*-tests, n=3. (**F-I**) Abundance levels (ion counts) of NADPH and GSH in GBM217gs and GBM374gs, measured via LC-MS. Two-way ANOVA, n=3. (**J-K**) ROS levels in GBM374gs and GBM217gs via CellROX. Two-way ANOVA, n=3. (**L**) Progression-free interval in PKM2-low and PKM2-high expressing GBM tumors.

Figure 5

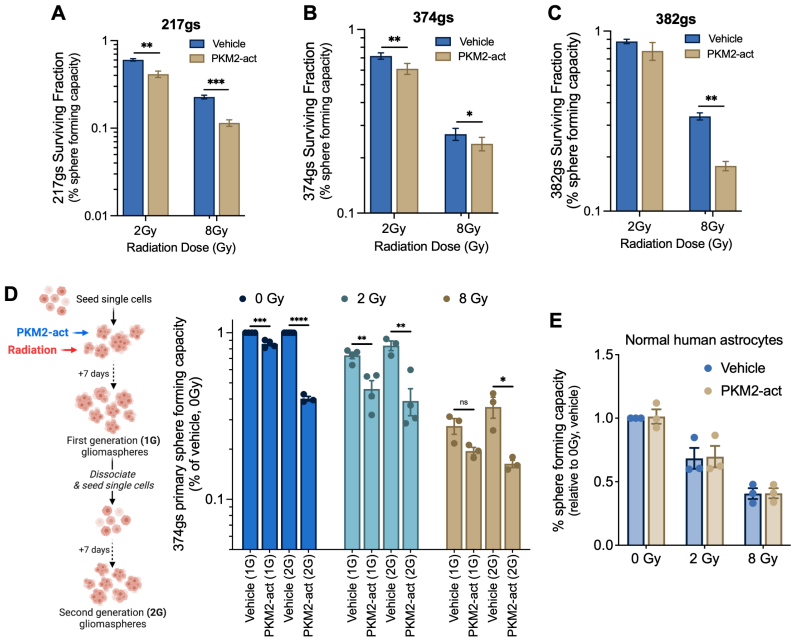

Figure 5. PKM2 activation radiosensitizes gliomaspheres *in vitro*. (**A-C**) Surviving fraction of gs determined via sphere forming capacity assays. Unpaired *t*-tests, n=3. (**D**) The spheres were then dissociated and re-seeded without further treatment and allowed to form secondary spheres (second generation, 2G). Unpaired *t*-tests, n=3. (**E**) Sphere forming capacity assay with normal human astrocytes. Unpaired *t*-tests, n=3.

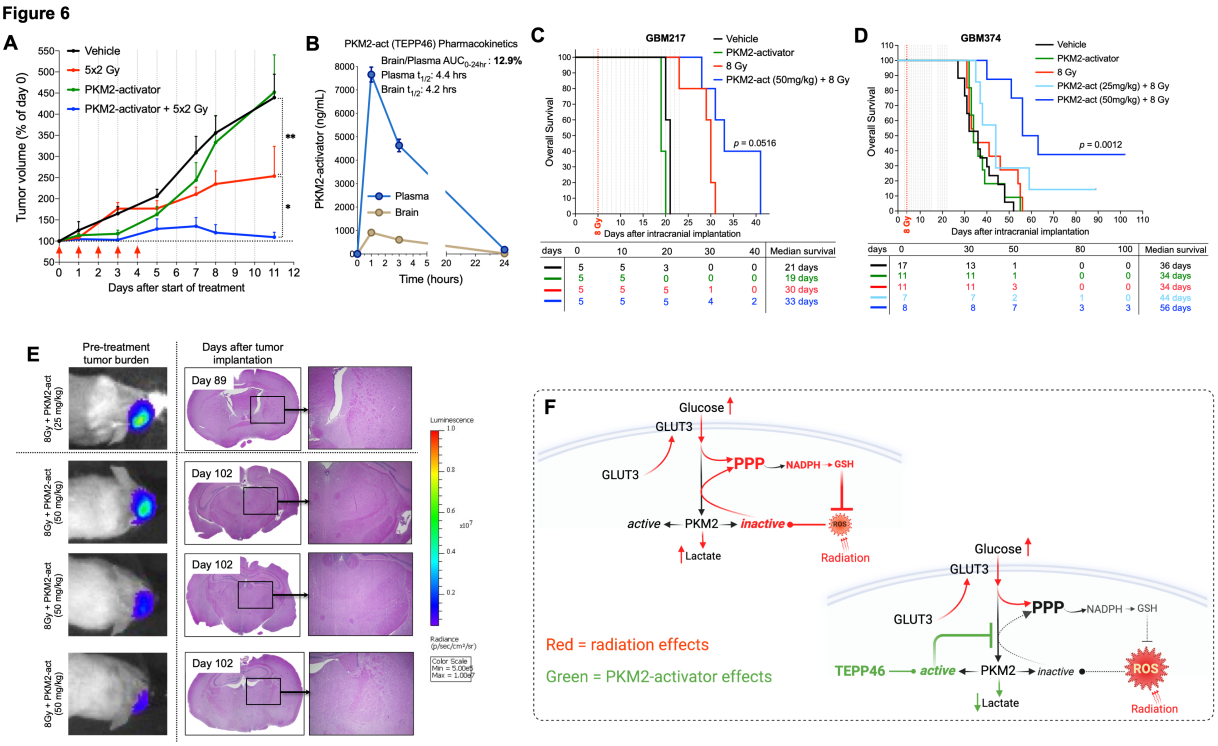

Figure 6. PKM2 activation radiosensitizes GBM tumors *in vivo*. (**A**) Tumor growth of GBM374 subcutaneous tumors, treated with 50 mg/kg TEPP46 (dotted vertical lines) and 2 Gy fractions of radiation (red arrows). Statistical analyses in the M&M section. (**B**) Pharmacokinetic analysis of TEPP46 levels in the plasma and the brain of TEPP46-treated (50 mg/kg), tumor-free NSG mice, determined by LC-MS. (**C-D**) Overall survival of mice bearing GBM374 and GBM217 intracranial tumors, via KM analysis (**D**), with endpoint as 'time to euthanasia' (time from tumor implantation to euthanasia). Dotted vertical lines: TEPP46 treatment days, red dotted vertical line: irradiation day. The difference in survival among these treatment groups was determined via log-rank test (p=0.001). Using Cox PH regression analysis, the difference in overall survival among treatment groups of GBM374 was also determined via LRT. See M&M for details. The table below indicates the number of mice still alive and well on a given day. (**E**) Luminescence images of long-term survivors' initial tumor burden, and hematoxylin/eosin IHC staining of brains at the time of

euthanasia. Right panels show zoomed-in images (4X) of the presumed tumor location. (**F**) Radiation increases glucose uptake in gliomaspheres, via increased membrane localization of GLUT3. Radiation also suppresses PKM2 activity, leading to a bottleneck in glycolytic flux and accumulation of glycolytic intermediates, promoting flux through the PPP, and the generation of antioxidants that have the potential to neutralize the oxidative stress induced by radiation. The use of PKM2-activators can prevent the suppression of PKM2 activity by radiation, thus antagonizing the antioxidant function of the PPP.

SUPPLEMENTARY FIGURES

Supplementary Figure 1 cont'.

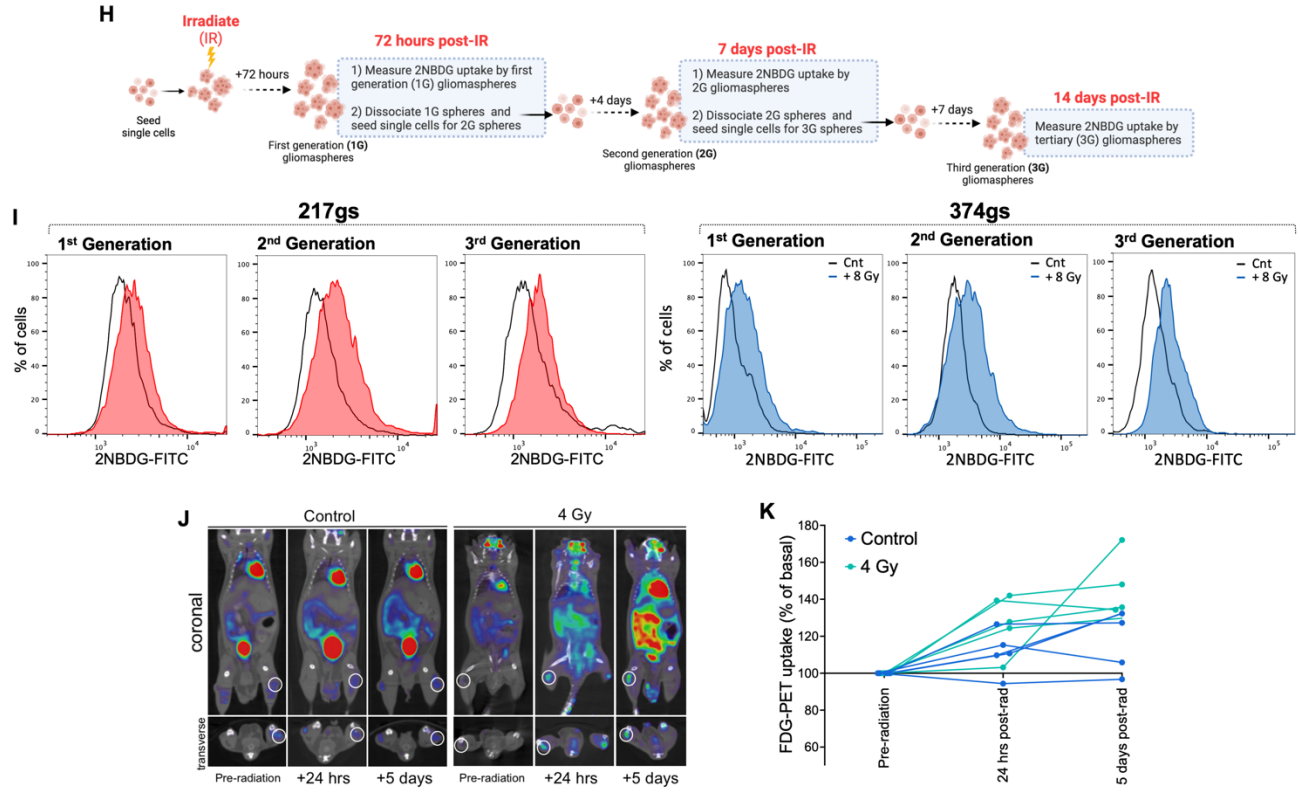

Supplementary Figure 1.

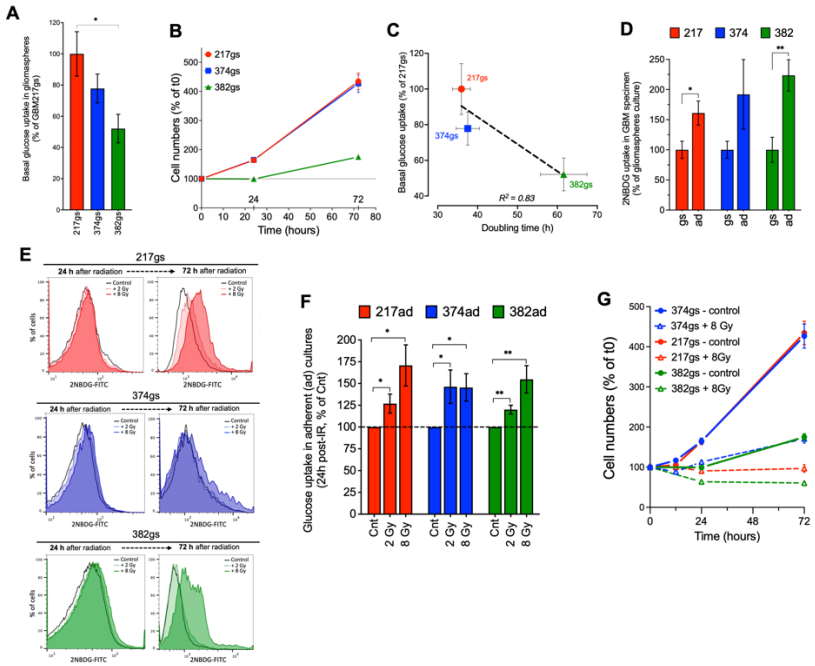

Supplementary Figure 1: (**A**) Basal glucose uptake measured via 2NBDG assay and analyzed via flow cytometry in GBM217, GBM374 and GBM382 grown as gliomaspheres (gs). Glucose uptake was normalized to GBM217 cells. Two-tailed unpaired t-tests were performed, n=5. (**B**) Cell proliferation of GBM217gs, GBM374gs and GBM382gs determined by counting cells at various timepoints after plating (t0), normalized to t0. (**C**) Correlation between doubling time and basal glucose uptake. (**D**) Basal glucose uptake measured via 2NBDG assay and analyzed via flow cytometry in GBM217, GBM374 and GBM382 grown as gliomaspheres compared to adherent cells. Glucose uptake was normalized to gliomasphere cultures. Two-tailed unpaired t-tests were performed, n=4. (**E**) Representative flow charts of 2NBDG assay at 24 h and 72 h after radiation in GBM217 (top panel, red), GBM374 (middle panel, blue) and GBM382 gliomaspheres (bottom panel, green). (**F**) Glucose uptake measured via 2NBDG assay and analyzed via flow cytometry in GBM217, GBM374 and GBM382 grown as adherent cells (ad), at 24 h after radiation with 2 Gy or 8 Gy. Glucose uptake was normalized to non-irradiated control (Cnt). Two-tailed unpaired t-tests were performed, n=4. (**G**) GBM217, GBM374 and GBM382 gliomaspheres were seeded as single cells, irradiated with a single dose of 8 Gy, and dissociated at 12 h, 24 h and 72 h post-radiation for cell counting to determine cell growth. Two-tailed unpaired t-tests were performed, n=3. (**H-I**) GBM374 and GBM217 gliomaspheres were plated as single cells, irradiated with a single dose of 8 Gy, and glucose uptake was measured via 2NBDG assay during the first sphere generation (1G) 72 h post-radiation, the second sphere generation (2G) 7 days post-radiation, and the third sphere generation (3G) 14 days post-radiation (**H**). Representative flow cytometry histograms are shown for each generation (**I**). (**J**) Representative images of FDG-PET and CT scan at different timepoints, in control and irradiated mice (4 Gy). (**K**) FDG uptake measured via PET scan in NSG mice injected in the tail vein with ^{18}F-FDG. FDG uptake levels were determined in all mice and used as basal levels to normalize follow up measurements in non-treated and irradiated mice.

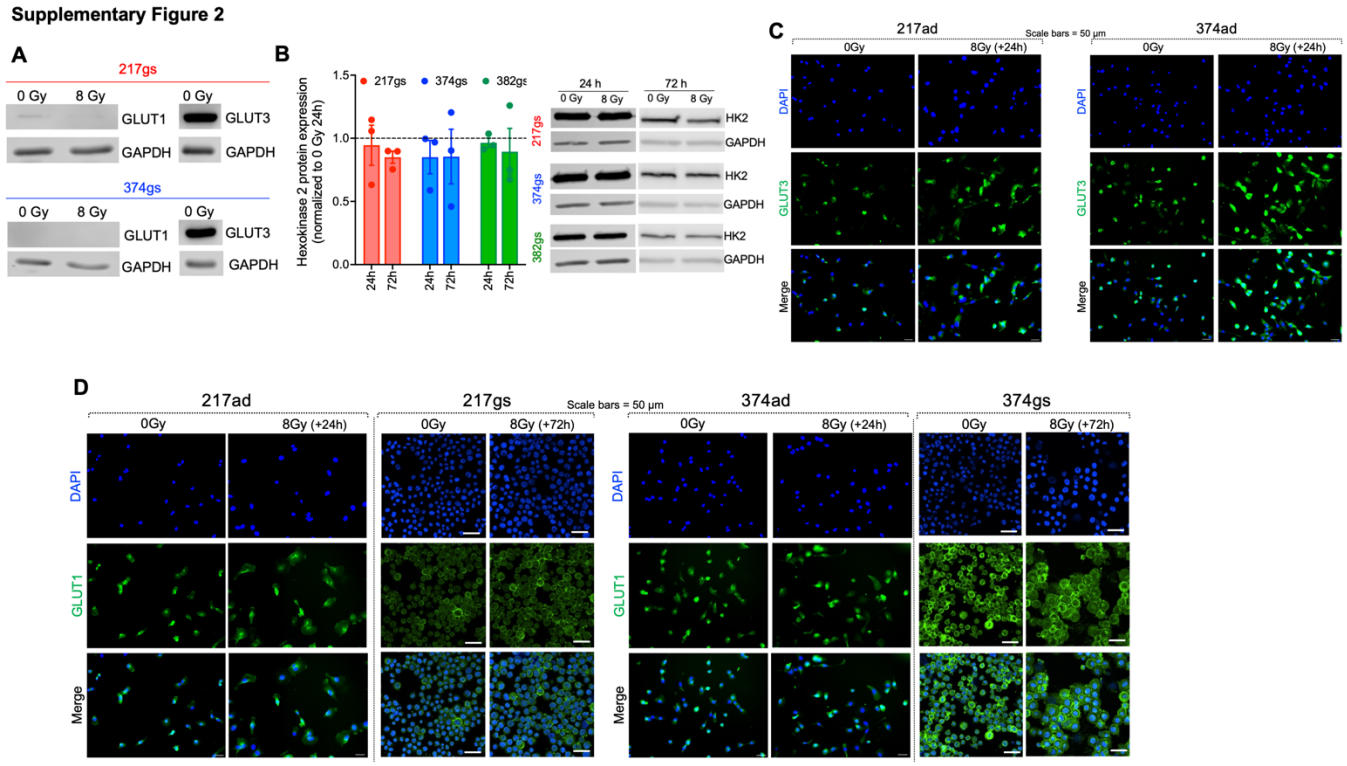

Supplementary Figure 2: (**A**) GLUT1/3 protein levels in GBM217gs and GBM374gs at basal levels and 24 h after radiation (GLUT1). (**B**) Hexokinase 2 protein expression measured by western blot in GBM217, GBM374 and GBM382 gliomaspheres at 24 and 72 h after radiation (2 or 8 Gy). GAPDH was used as a loading control (right panel), n=3/4. (**C**) Cell surface GLUT3 protein was stained via immunocytochemistry in adherent GBM217 and GBM374 cells, at 24 h after radiation (8 Gy). Images were captured on a Keyence BZ-9000 microscope at 20x. The scale bar equals 50 µm. (**D**) Cell surface GLUT1 protein was stained via immunocytochemistry in adherent and suspension GBM217 and GBM374 cells, at 24 and 72 h after radiation (8 Gy). Images were captured on a Keyence BZ-9000 microscope at 20x (ad) and confocal microscope at 40x (gs). The scale bar equals 50 µm.

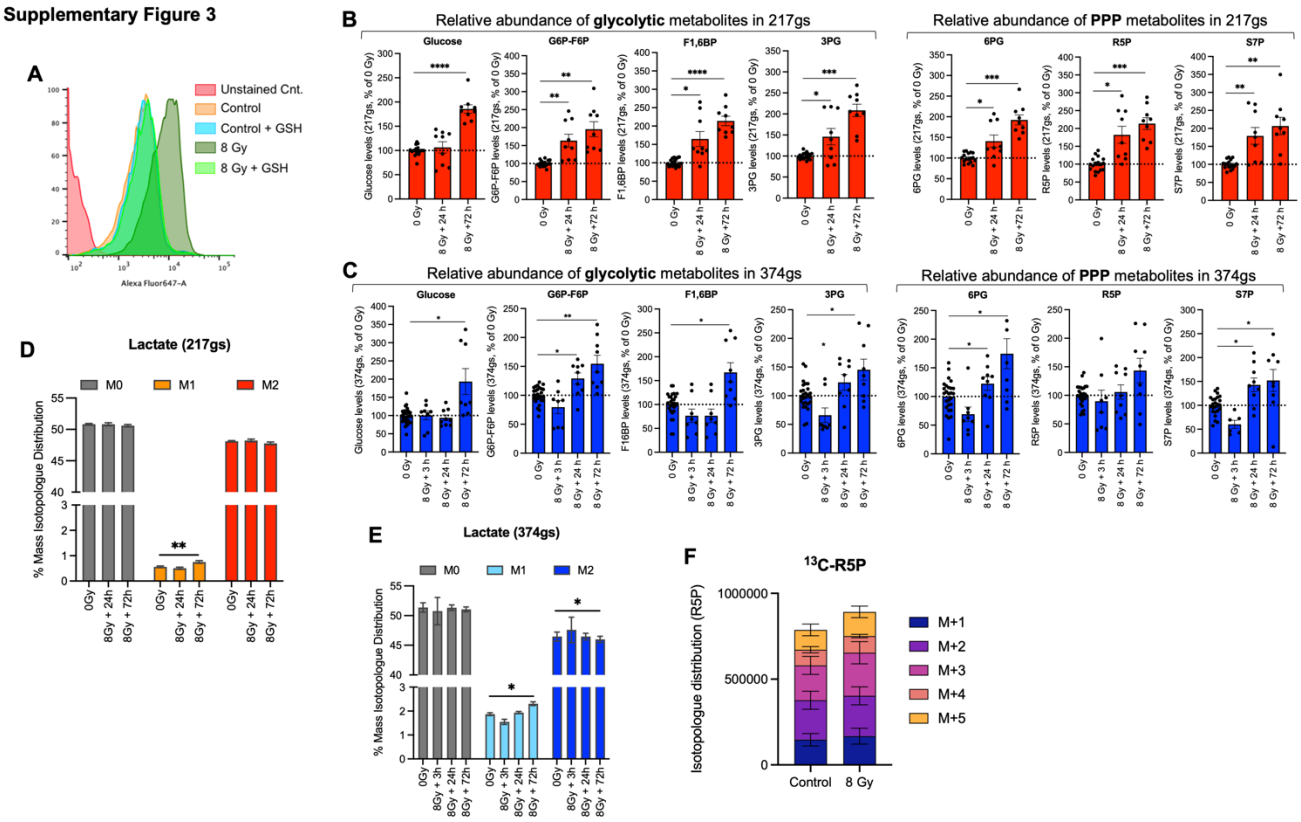

Supplementary Figure 3: (**A**) Representative flow charts of CellROX assay (AlexaFluor-647) in GBM374 gliomaspheres, at 24 h after radiation and in the presence of GSH. (**B-C**) Bar graphs of glycolytic and PPP metabolites at 24 and 72 h after radiation in GBM217gs (**B**) and GBM374gs (**C**). Two-tailed paired t-tests were performed, n=3. (**D-E**) Mass Isotopologue Distribution of lactate in GBM217gs (**D**) and GBM374gs (**E**). Two-tailed paired t-tests were performed, n=3. (**F**) Isotopologue distribution of R5P measured by LC-MS, in U-^{13}C-glucose infused brain tissues.

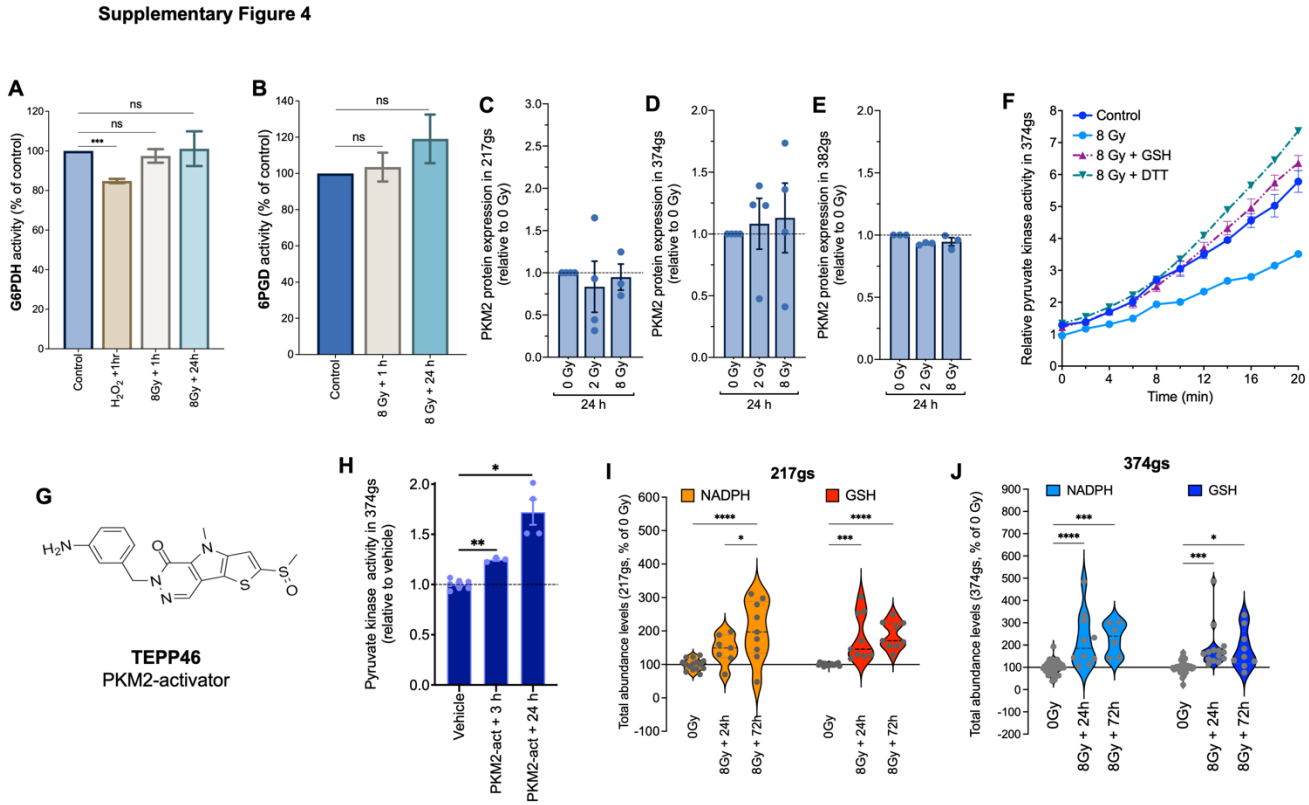

Supplementary Figure 4: (**A**) G6PDH activity measured in GBM374gs cells, via G6PDH assay kit, after 500 µM H_2O_2 treatment (1 h) or 1 h and 24 h post-radiation treatment (8 Gy). Two-tailed unpaired t-tests were performed, n=3. (**B**) 6PGD activity measured in GBM374gs cells, via 6PGD assay kit, 1 h and 24 h post-radiation. Two-tailed unpaired t-tests were performed, n=3. (**C-E**) PKM2 protein expression measured by western blot in GBM217, GBM374 and GBM382 gliomaspheres at 24 h after radiation (2 or 8 Gy). GAPDH was used as a loading control, n=3/4. (**F**) Pyruvate kinase activity in GBM374gs after radiation, and in the presence of DTT (1 mM) or GSH (5 mM) added prior to radiation. (**G**) Chemical structure of TEPP46. (**H**) Pyruvate kinase activity measured in GBM374gs cells treated with a PKM2-activator (TEPP46, upper panel). Two-tailed unpaired t-tests were performed, n=3. (**I-J**) Abundance levels (ion counts) of NADPH and GSH in GBM217gs and GBM374gs, measured via LC-MS. Two-way anova, n=3.

Supplementary Figure 5

A

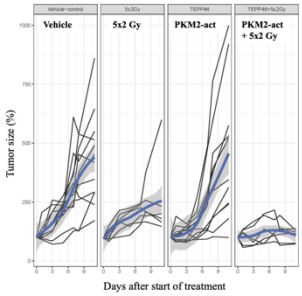

B

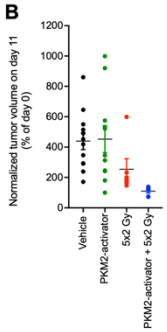

C

Interaction effects in linear mixed-effects model*

**Main effect of day and treatment are not listed in the table*

Reference group: vehicle	Estimate	Std. Error	df	t value	Pvalue
day: 5x2 Gy	**-18.15**	**4.75**	**194.27**	**-3.82**	**<0.001**
day: PKM2-act	-0.64	4.00	194.39	-0.16	0.87
day: PKM2-act + 5x2 Gy	**-30.94**	**4.73**	**194.15**	**-6.54**	**<0.001**

Reference group: 5x2 Gy	Estimate	Std. Error	df	t value	Pvalue
day: Vehicle	**18.15**	**4.75**	**194.27**	**3.82**	**<0.001**
day: PKM2-act	**17.50**	**4.74**	**193.83**	**3.69**	**<0.001**
day: PKM2-act + 5x2 Gy	**-12.79**	**5.37**	**193.77**	**-2.38**	**0.02**

Reference group: PKM2-act	Estimate	Std. Error	df	t value	Pvalue
day: 5x2 Gy	**-17.50**	**4.74**	**193.83**	**-3.69**	**<0.001**
day: Vehicle	0.64	4.00	194.39	0.16	0.87
day: PKM2-act + 5x2 Gy	**-30.29**	**4.72**	**193.68**	**-6.42**	**<0.001**

Reference group: PKM2-act + 5x2 Gy	Estimate	Std. Error	df	t value	Pvalue
day: PKM2-act	**30.29**	**4.72**	**193.68**	**6.42**	**<0.001**
day: 5x2 Gy	**12.79**	**5.37**	**193.77**	**2.38**	**0.02**
day: Vehicle	**30.94**	**4.73**	**194.15**	**6.54**	**<0.001**

Likelihood ratio test (LRT): model w/ interaction term *vs* model w/o interaction term

	logLik	deviance	Chisq	Df	Pr(>Chisq)
Model w/o interaction term	-1423.74	2847.48	NA	NA	NA
Model w/ interaction term	-1397.75	2795.49	51.99	3.00	<0.001

D

ANOVA	Df	Sum Sq	Mean Sq	F value	Pr(>F)
Treatment	3.00	612541.83	204180.61	4.47	0.01
Residuals	31.00	1415800.32	45670.98	NA	NA

Post-hoc Tukey-HSD	difference	Lower bound of 95% Confidence interval	Upper bound of 95% confidence interval	p adj
Vehicle *vs.* PKM2-act	-12.83	-254.94	229.28	1.00
Vehicle *vs.* 5x2 Gy	185.54	-104.47	475.55	0.32
Vehicle *vs.* PKM2-act + 5x2 Gy	**329.93**	**39.92**	**619.93**	**0.02**
5x2 Gy *vs.* PKM2-act	198.37	-96.00	492.74	0.28
5x2 Gy *vs.* PKM2-act + 5x2 Gy	-144.38	-479.26	190.49	0.65
PKM2-act *vs.* PKM2-act + 5x2 Gy	**-342.75**	**-637.12**	**-48.38**	**0.02**

E

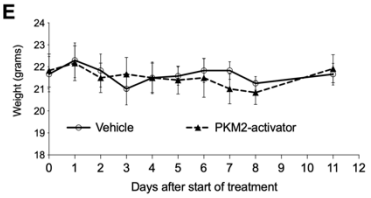

F

Obtained from KM analysis GBM374	median survival (days)	lower bound	upper bound
Vehicle	36	30	41
8 Gy	34	31	54
PKM2-act (50 mg/kg)	34	32	39
8 Gy + PKM2-act (25 mg/kg)	44	35	59
8 Gy + PKM2-act (50 mg/kg)	56	28	NA

Cox PH regression *Reference group: 8 Gy*	HR	Lower CI	Upper CI	*P* value
vehicle vs. 8 Gy	1.94	0.81	4.67	0.14
PKM2-act (50 mg/kg) vs. 8 Gy	1.67	0.65	4.29	0.28
8 Gy + PKM2-act (25 mg/kg) vs. 8 Gy	0.41	0.14	1.20	0.10
8 Gy + PKM2-act (50 mg/kg) vs. 8 Gy	**0.23**	**0.08**	**0.69**	**<0.01**
Weight	*1.05*	*0.94*	*1.18*	*0.37*

Likelihood ratio test (LRT): model w/ tx vs model w/o tx

	loglik	Chisq	Df	pvalue
Model w/ tx	-154.52	NA	NA	NA
Model w/o tx	-164.96	20.87	4.00	<0.001

G

Pairwise comparison via log-rank test GBM217	PKM2-act	PKM2-act + 8 Gy	Vehicle
PKM2-act + 8 Gy	<0.01	NA	NA
Vehicle	0.02	<0.01	NA
Vehicle + 8 Gy	<0.01	0.05	<0.01

Supplementary Figure 5, cont'

H

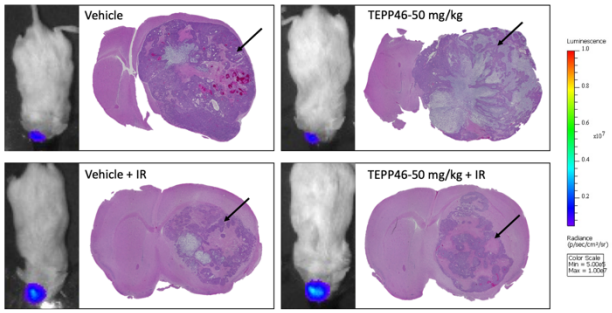

Supplementary Figure 5, cont'

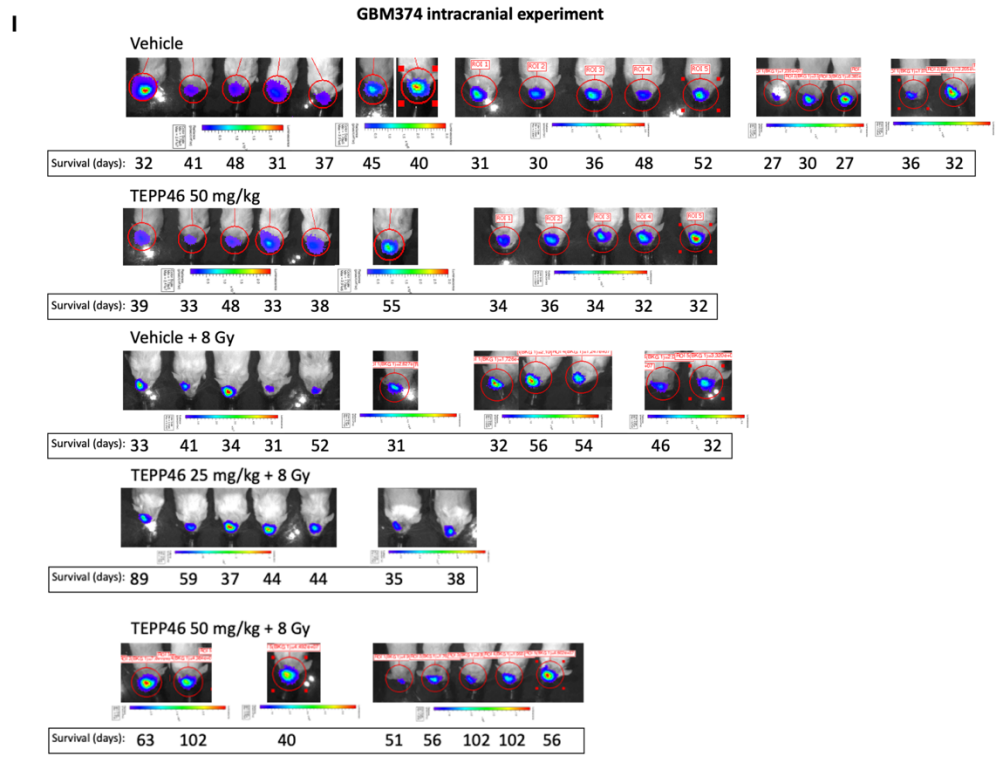

Supplementary Figure 5: (**A**) Spaghetti plots: a black curve indicates the time trend for tumors at each location on the mouse. The blue curve indicates the general time trend for the respective treatment group. The general time trend among 4 treatments seems to differ via visual inspection. The time trend for vehicle and PKM2-act appears to be the steepest, 5x2 Gy to be the 2nd steepest and PKM2-act+5x2 Gy seems to have the least steep time trend. (**B**) Subcutaneous GBM374 tumor volumes on day 11 after beginning of treatment, normalized to first day of treatment. (**C**) The time effect (growth rate per day) was found to be different among treatment groups via LRT within linear mixed-effects model. Considering 5x2 Gy as the reference group, the vehicle and PKM2-act groups were found to have a more positive growth rate per day (steeper) and PKM2-act+5x2 Gy was found to have a more negative growth rate per day (less steep). (**D**) Differences in tumor sizes at day 11 among treatment groups were identified via ANOVA, followed by post-hoc analysis with TukeyHSD test, which identified specific differences in tumor sizes between pairs of PKM2-act+5x2 Gy vs. PKM2-act and vehicle vs. PKM2-act+5x2 Gy. (**E**) Mice weights measured every day in vehicle and TEPP46 (PKM2 activator) treated mice. (**F-G**) Kaplan-Meier statistical analysis of survival of mice bearing GBM374 and GBM217 tumors. The difference in survival among these treatment groups was determined via log-rank test (p=0.001). Using Cox PH

regression analysis, the difference in overall survival among treatment groups was also determined via LRT. See Material and Methods for details. (**H**) Hematoxylin/eosin IHC staining of tumor-bearing NSG brains at the time of euthanasia, from Vehicle, Vehicle + IR, TEPP46 (50 mg/kg) and TEPP46 + IR groups. A black arrow indicates a tumor. (**I**) Bioluminescence images of GBM374 tumor-bearing mice 3 days after implantation in the brain. The table below indicate the survival time in days.

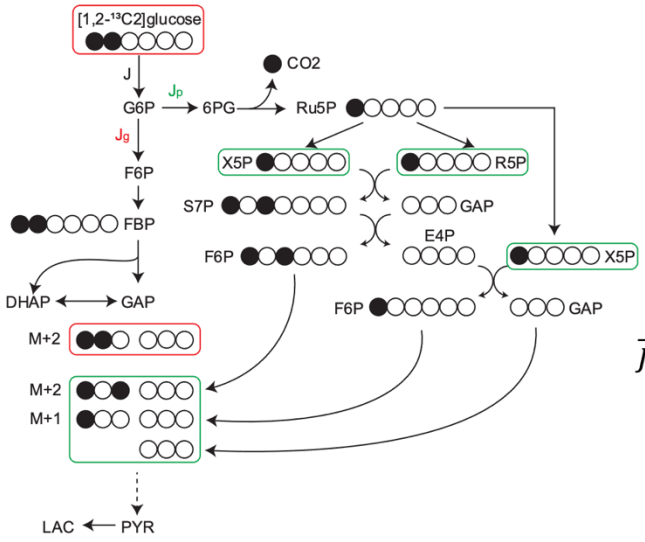

$$\frac{f_{M+2}}{f_{M+1}} = \frac{\frac{1}{5}J_p + \frac{1}{2}J_g}{\frac{1}{5}J_p} = \frac{2J_p + 5J_g}{2J_p} = 1 + \frac{5}{2}\frac{J_g}{J_p} \dots eq.1$$

$$\frac{J_g}{J_p} = \frac{2}{5}\left(\frac{f_{M+2}}{f_{M+1}} - 1\right) \dots eq.2$$

$$\frac{J_p}{J_p + J_g} = \frac{1}{1 + \frac{J_g}{J_p}} = \frac{1}{1 + \frac{2}{5}\left(\frac{f_{M+2}}{f_{M+1}} - 1\right)} = \frac{5\frac{f_{M+1}}{f_{M+2}}}{2 + 3\frac{f_{M+1}}{f_{M+2}}} \dots eq.3$$

$$J_p = glucose\ uptake\ flux * \frac{5\frac{f_{M+1}}{f_{M+2}}}{2 + 3\frac{f_{M+1}}{f_{M+2}}} \dots eq.4$$

Supplementary Figure 6: Calculation of fraction in glucose uptake flux (J) that goes to oxidative pentose phosphate pathway (oxPPP) based on ^{13}C- labeling fraction of lactate. Glucose uptake flux (J) is fractioned into glycolysis (Jg) and oxPPP flux (Jp). 1 glucose molecule generates 1 GAP(M+2) and 1 GAP(M+0) via glycolysis (red box), and 3 glucose molecules become 3 pentose phosphate(M+1) molecules and generate 1 GAP(M+2), 1 GAP(M+1) and 3 GAP(M+0) via oxPPP (green box). 50% of glycolysis flux and 20% of oxPPP flux generate GAP(M+2) and 20% of oxPPP flux generates GAP(M+1). Thus, the fraction of lactate(M+2) over lactate(M+1) is expressed as eq.1. After rearranging, ratio of glycolytic flux divided by oxPPP flux is expressed as eq.2. As glucose uptake rate is the sum of the glycolytic and oxPPP flux, fraction

of glucose uptake flux that goes to oxPPP is expressed as eq.3. OxPPP flux is expressed as glucose uptake flux and ^{13}C- labeling fraction of lactate (eq.4).

Authorship:
Conceptualization: JB, AJS, JOP, DSc, WHM, DRW, EV
Data curation: JB, YR, AJS, TY, LA, HH, DSu, JN, DP, AS, JET, JOP, JtH, NQ
Formal analysis: JB, YR, KP, AJS, TY, LA, HH, DSu, JN, FC, JET, JOP, CAL, DRW, EV
Funding acquisition: EV, DRW
Investigation: JB, YR, KP, AJS, TY, DS, JN, DP, AS, JET, SX, JtH, KB, NQ
Methodology: JB, KP, AJS, JET, SX, JOP, JtH, KB, NQ, CAL, DRW, EV
Project administration: JB, EV
Resources: JET, DAN, SX, JOP, JtH, KB, NQ, HIK, CAL, DRW
Supervision: JB, EV
Validation: JB, EV
Visualization: JB, AJS, SX, JOP, DS, WHM, DRW, EV
Writing – original draft: JB, YR, KP, AJS, FC, JET, SX, JOP, JtH, EV
Writing – review & editing: JB, AJS, DSu, FC, DAN, SX, JOP, JtH, KB, HIK, DSc, WHM, DRW, EV

Supplementary Material & Methods

Cell culture: Primary human glioblastoma lines, GBM217, GBM374, GBM382 were established at the University of California, Los Angeles (UCLA) as described in Laks *et al.*[1]. All GBM specimens used in this study were IDH-wt, primary, treatment-naïve gliomas, that were chosen for their differences in growth rates and in PTEN and EGFR status: GBM217 (no EGFR amplification, EGFRvIII-neg, PTEN-neg), GBM374 (EGFR amplification, EGFRvIII-pos, PTEN-pos), GBM382 (no EGFR amplification, EGFRvIII-neg, PTEN-pos). The cells were propagated as gliomaspheres (unless stated otherwise) in DMEM/F12 media (ThermoFisher). DMEM/F12 was supplemented with SM1 (StemCell Technologies), 4 μg/mL heparin (Sagent, Schaumburg, IL), 20 ng/mL fibroblast growth factor 2 (bFGF) (StemCell Technologies), 20 ng/mL epidermal growth factor (EGF) (StemCell Technologies) and Penicillin/Streptomycin cocktail (ThermoFisher) (hereafter referred to as "GBM media"). Propagation as gliomaspheres required the use of non-treated tissue culture plates and flasks. When grown as adherent monolayers, the cells were cultured in DMEM (ThermoFisher), supplemented with 10% fetal bovine serum (FBS) (Sigma-Aldrich) and Penicillin/Streptomycin cocktail. Patient-derived xenografts (GBM38)[2] were provided by Dr. Jann Sarkaria (Mayo Clinic). GFP^+fluc^+ tissues were produced by infecting short-term explant GBM38 cultures with lentiviruses harboring GFP and luciferase (lenti-LEGO-Ig2-fluc-IRES-GFP-VSVG) and then enriching GFP^+ cells by FACS. Cells were then injected subcutaneously into the flanks of female Rag1 KO mice (B6.129s7-RAG1 tm/Mom/J, Jackson Laboratory) to propagate GFP^+ GBM tissue. Normal Human Astrocytes (NHA) were obtained from Dr. Nathanson's lab and grown in DMEM supplemented with 10% FBS and Penicillin/streptomycin cocktail. All cells were grown at 37°C, in a humidified incubator with 5% CO_2.

Irradiation and treatments: Cells were irradiated at room temperature using an experimental X-ray irradiator (Gulmay Medical Inc, Suwanee, GA) at a dose rate of 7.1702 Gy/min. The X-ray beam was operated at 300 kV and hardened using 4-mm Be, 3-mm Al, and 1.5-mm Cu filters. Corresponding controls were sham irradiated. Dosimetry was standardized to NIST using ion chambers and film. Unless otherwise stated, cells were treated with 10 μM of the PKM2 activator,

TEPP46 (MedChem Express) 3 hours prior to irradiation. 2-Deoxy-D-Glucose, 2DG (Sigma) was used at a dose of 5 mM in glucose-free complete GBM media, 2 hours prior to irradiation. GSH-MEE (Sigma) was used at 5 mM, 5 minutes prior to irradiation.

Gliomasphere formation assay (SFA): Gliomasphere-forming capacity was determined by plating single cells in GBM media (see "GBM cells and cell culture"), into 96-well non-treated plates, at a range of cell densities appropriate for the different cell lines and doses of radiation. Fresh media was added every 3 days. 48 hours after cell seeding, cells were treated with TEPP46 (10 μM) every day for 5 days. Irradiation was performed 3 hours after the first drug treatment. The number of spheres formed per well was counted 7 to 10 days after plating. Spheres were then dissociated and reseeded as single cells to form a second generation of spheres (2G). The surviving fraction was determined as previously described[3] by normalizing the number of spheres formed to the number of cells initially plated.

Glucose uptake assay: $2x10^5$ cells/well were plated in 6-well plates, as gliomaspheres or as monolayers allowed to adhere overnight, and treated and/or irradiated the next day. The fluorescent glucose analogue 2-deoxy- 2-[(7-nitro-2,1,3-benzoxadiazol-4-yl)amino]-d-glucose, 2NBDG (ThermoFisher) was used for measuring glucose uptake. 24 and 72 hours after irradiation, monolayer cells were removed by trypsinization and gliomaspheres were dissociated with accutase. Cells were then incubated for 30 minutes with 100 μM 2NBDG in glucose-free media at 37°C. After washing away free 2NBDG, cells were then resuspended in PBS, and analyzed by flow cytometry and the geometrical mean fluorescence was determined. Correlation of glucose uptake with cell growth was determined by calculating the doubling time of each cell line.

Determination of glucose uptake and lactate production rates via YSI: Media from gliomaspheres was collected and processed in a biochemistry analyzer (YSI 2950D, Xylem Inc., Ohio, USA) in 96-well plates. The plates were placed in the YSI 2950D for batch sampling and measurement with biosensor probes with glucose (2365) and lactate (2329) membranes (Xylem Inc.). The median value of three technical replicates was selected for analysis.

The concentration of the samples was calculated using the following formula:

$$[glucose]\ [gL^{-1}] = 3C_{glucose}\ k_{glucose}e$$
$$[lactate]\ [gL^{-1}] = 3C_{lactate}\ k_{lactate}e$$

where e is the ratio of the glucose concentration of control media sample at 0 hour to those at the other time points, k is the slope of the calibration curve, and C is the measured concentration.

The following formula was then used to calculate glucose uptake rate $[nmol\ (million\ cells)^{-1}\ hr^{-1}]$ between time t_1 and t_2:

$$glc\ uptake\ rate = -\frac{sl(t_1,t_2)\ [gL^{-1}hr^{-1}] * 0.002[L] * \frac{1[mol]}{180[g]} * \frac{10^9[nmol]}{1[mol]}}{AVCN(t_1,t_2)[cells] * \frac{1[million\ cells]}{10^6[cells]}}$$

where $sl(t_1,t_2)\ [gL^{-1}hr^{-1}]$ is the slope value between t_1 and t_2 and $AVCN(t_1,t_2)\ [cells]$ is the average cell number in the time interval t_1-t_2.

The lactate secretion rate $[nmol\ (million\ cells)^{-1}\ hr^{-1}]$ between t_1 and t_2 was calculated using the following formula:

$$lac\ uptake\ rate = \frac{sl(t_1, t_2)\ [gL^{-1}hr^{-1}] * 0.002[L] * \frac{1[mol]}{90[g]} * \frac{10^9[nmol]}{1[mol]}}{AVCN(t_1, t_2)[cells] * \frac{1[million\ cells]}{10^6[cells]}}$$

ROS detection: Gliomaspheres were seeded as single cells and treated with a drug or vehicle. Gliomaspheres were then dissociated at the appropriate time with accutase (Innovative Cell Technologies), counted, and $2x10^5$ cells were allocated per condition. Staining was performed prior to irradiation, by incubating the cells with 5 μM of CellROX-deep red reagent (ThermoFisher Scientific) in GBM media, for 30 minutes at 37°C, protected from light. After one PBS wash, cells were then irradiated or not, and analyzed by flow cytometry (BD LSR Fortessa). Data were analyzed with FlowJo 10, and the geometrical mean fluorescence was determined. The results were normalized to the unirradiated control.

G6PDH and 6PGD activity assay: Cells were plated as single cells and treated the following day with TEPP46 3 hours prior to radiation. 500 μM H_2O_2 was added 1 hour prior to the extraction. The G6PDH levels were measured using the G6PDH Activity Assay Kit (Cell Biolabs) according to the manufacturer's protocol. The 6PGD activity levels were measured using the 6-Phosphogluconate Dehydrogenase Assay Kit (Abcam). Cells were collected and lysed 1 hour or 24 hours after radiation according to the manufacturer's instructions. The samples were read at 450 nm (G6PDH activity) and 460 nm (6PDG activity) OD on a plate reader (SpectraMax M5, Molecular Devices, Sunnyvale, CA). The levels of G6PDH and 6PGD activity were determined by comparing the OD values to the standard curve.

Pyruvate kinase activity assay: Pyruvate kinase activity assays were performed as previously described[4]. Single cell suspensions of GBM cells propagated as monolayers or gliomaspheres were seeded in duplicates on 24-well tissue culture-treated or non-treated plates. The cells were placed in the incubator overnight and the next day treated with either 5 mM GSH-MEE 5 minutes before radiation, 10 μM TEPP46 3 hours before radiation and/or 8 Gy. Cells were removed from one set of the wells from each treatment group and the number of viable cells was determined via a hemocytometer via trypan blue staining. The other set of wells was used for determination of pyruvate kinase activity in each group via the Pyruvate Kinase Assay kit (Abcam, #ab83432) according to the manufacturer's instructions. Briefly, cells were washed once with PBS, followed by addition of pyruvate kinase assay buffer to each well for cell lysis. The cell lysate mixture was diluted to contain 2000 cells / 50 μL (based on the cell numbers obtained with the trypan blue counting) with assay buffer. 50 μL of the cell lysate from each group was transferred on 96-well plates. Then, 50 μL of the master reaction mix was added to each sample. A fraction of the cell lysate was treated with 1 mM of dithiothreitol (DTT, Sigma-Aldrich). The optical density (OD 570 nm) was measured as a function of time using a plate reader (SpectraMax M5, Molecular Devices, Sunnyvale, CA) at room temperature every minute for a total of 15 minutes. The signal increase per unit of time correlates with the amount of pyruvate generated by pyruvate kinase. Two OD570nm values (A1 and A2) within the linear range of the reaction for each sample were identified. The $\Delta A = A2 - A1$ was determined and plotted for each group.

TCGA analysis: Gene expression levels of PKM2 in the TCGA Glioblastoma database were correlated with progression-free interval using UCSC Xena (https://xenabrowser.net/) to generate Kaplan-Meyer survival curves for PKM2-low and PKM2-high expressing GBM.

***In vitro* Metabolomics:**

Metabolite extraction: Gliomaspheres were incubated with complete media containing 17.5 mM [1,2-$^{13}C_2$]-glucose (99%) (Cambridge Isotope Laboratories). Metabolites were extracted at 3, 24 or 72 h post-IR, for a labeling time of 24, 48 or 96 h, respectively, with replenishment to avoid media exhaustion. Extraction was performed as previously described[5], with 80% methanol 0.1 M formic acid at -80°C, and neutralized with 15% (w/v) ammonium bicarbonate.

Metabolite measurement by LC-MS: The metabolites were loaded onto a Luna 3um NH2 100A 150 × 2.0 mm column (Phenomenex). The chromatographic separation was performed on a Vanquish Flex (Thermo Scientific) with mobile phases A (5 mM ammonium acetate buffer at pH 9.9) and B (acetonitrile) and a flow rate of 200 µL/min. A linear gradient from 15% A to 95% A over 18 minutes was followed by 9 min isocratic flow at 95% A and re-equilibration to 15% A. Metabolites were detected with a Thermo Scientific Q Exactive mass spectrometer run with polarity switching (+3.5 kV/− 3.5 kV) in full scan mode with an m/z range of 70-975. TraceFinder 4.1 (Thermo Scientific) was used to quantify metabolites by area under the curve using expected retention time and accurate mass measurements (< 5 ppm). The ^{13}C labeling measurements from LC-MS were corrected to account for natural ^{13}C isotope abundance and ^{12}C impurity present in the ^{13}C-glucose tracers[6].

***Analysis of metabolite levels and isotope labeling*:** To calculate PPP flux variation between conditions, we retrieved M+1 (singly labeled) and M+2 (doubly labeled) lactate intensities after correcting for ^{13}C natural abundance. The absolute PPP flux [*nmol (million cells)$^{-1}$ hr^{-1}*] was calculated with the following formula (Supplementary Figure 6):

$$glucose\ uptake\ rate\ (t_1) * \frac{5 * \frac{M+1}{M+2}}{(2 + \left(3 * \frac{M+1}{M+2}\right))}$$

We used glucose uptake rate from 0 to 12 hours, 12 to 48 hours, and 24 to 72 hours to calculate the PPP flux at 3 hours, 24 hours, and 72 hours, respectively.

Immunofluorescence (IF) for glucose transporters *via* flow cytometry:

Glucose transporters IF was performed as follows: after 4% paraformaldehyde (PFA, VWR) fixation for 15 minutes and 10% goat serum blocking for 30 minutes at room temperature, the cells were incubated with the following antibodies for 1 hour at room temperature in the dark: human GLUT1-Alexa Fluor 405 (R&D Systems, 1:400, FAB1418V-100UG), human GLUT3-Alexa Fluor 647 (R&D Systems, 1:400, FAB1415R-100UG), mouse IgG2B-Alexa Fluor 405 (R&D Systems, 1:400, IC0041V) or mouse IgG2B-Alexa Fluor 647 (R&D Systems, 1:400, IC0041R). Analysis was performed on a flow cytometer (BD LSR Fortessa). Data were analyzed with FlowJo 10, and the geometrical mean fluorescence was determined. The results were normalized to the isotype controls and the unirradiated control.

Glucose Transporters immunocytochemistry (ICC):

GBM cells were either grown as adherent cells in chamber slides (Nunc, Lab-Tek, Thermo Fisher Scientific), or as gliomaspheres in non-treated flasks. The cells were irradiated, and at the

appropriate time after radiation, cells were processed for immunocytochemistry. For gliomaspheres cells, a single cell suspension was obtained, and 50,000 cells were deposited on a glass slide via Cytospin. The protocol is then identical for adherent and suspension cells: cells were washed with PBS and fixed with 4% paraformaldehyde at 37°C for 10 minutes and chilled on ice for 1 minute. Blocking was performed with 10% goat serum, for 30 minutes at room temperature under agitation. GLUT1 (ab115730, rabbit, 1:100; Abcam) and GLUT3 (ab191071, rabbit, 1:100; Abcam) primary antibodies were incubated for 30 minutes at room temperature, under agitation. Secondary antibody (anti-rabbit IgG-FITC, ab6717, 1:1000; Abcam) was added and incubated in the dark at room temperature for 30 minutes. Lastly, cells were counterstained with DAPI (Thermo Fisher Scientific). Images were taken with Keyence BZ-9000 fluorescent microscope (Keyence Corporation of America) and Confocal Scanning Microscope (A1 Nikon). Image analysis was performed with FIJI2 (previously ImageJ) software.

Protein extraction, cell fractionation and western blotting:
Whole cell proteins were extracted from cells at various time points after treatments. Briefly, cells were collected in 15 mL tubes, washed with PBS, and incubated for 30 minutes under agitation at 4°C in RIPA buffer (Abcam). Cell lysates were then centrifuged for 20 minutes at 12,000 rpm at 4°C and supernatants were collected.
Cell fractionation into membrane proteins and cytosolic proteins was achieved with Mem-PER Plus Membrane Protein Extraction Kit (ThermoFisher), according to the manufacturer's instructions. Briefly, cells were collected and washed with the Cell Wash Solution. After centrifugation, the cell pellet was resuspended with 0.75 ml of Permeabilization Buffer and incubated at 4°C for 10 minutes under agitation. Permeabilized cells were then centrifuged for 15 minutes at 15,000 rpm and the supernatant containing the cytosolic proteins was collected into a separate tube. The cell pellet containing the membrane proteins was resuspended with 0.5 ml of Solubilization Buffer and incubated 30 minutes at 4°C under agitation. Tubes were centrifuged for 15 minutes at 15,000 rpm and the supernatant containing membrane proteins was collected into a separate tube.
Protein concentrations were determined by Pierce BCA protein assay (ThermoFisher). Laemmli buffer (Bio-Rad) and 2-mercaptoethanol (Sigma) (350 mM) were added to the protein samples. Finally, proteins were denatured by heating the samples at 95°C for 5 minutes.
The extracted proteins were separated on 10% SDS-PAGE gels and transferred to PVDF membranes (ThermoFisher). Blots were incubated overnight with the primary antibodies against PKM2 (#21578, 1:1000, Signalway Antibody), GLUT1 (MAB14181, 1:1000, R&D Systems), GLUT3 (ab191071, 1:1000, Abcam), Hexokinase 2 (ab209847, 1:1000, Abcam) and GAPDH (#AM4300, 1:5000, Ambion). The membranes were then incubated with secondary antibodies conjugated to horseradish peroxidase (HRP) (Santa Cruz Biotechnology) for 1 hour at room temperature. The protein band detection was performed with ECL (Genesee Scientific) on an Odyssey Fc imaging system (Li-COR). Three biologically independent experiments were performed for each experimental group.

RNA extraction and real-time quantitative polymerase chain reaction (RT qPCR)
RNA was isolated from cells with TRIzol reagent (Ambion) according to the manufacturer's recommendations. RNA levels were measured with Nanodrop spectrophotometer (ThermoFisher). Complementary DNA synthesis was performed on 1 µg of isolated RNA by using cDNA synthesis kit (Genesee Scientific). Quantitative PCR was done with qPCR-BIO SyGreen Mix lo-ROX

(Genesee Scientific) according to manufacturer's instructions. Primers were purchased from ThermoFisher and can be found in Supplementary table 1.

Subcutaneous tumor models in mice: GBM374 cells were suspended in a solution of 1:1 mixture of Matrigel® basement membrane matrix (Corning) and DMEM medium supplemented with 10% FBS and 50,000 cells were injected subcutaneously in the hind legs of 5-week-old female NOD-*scid* IL2Rgamma^{null} (NSG) gnotobiotic mice bread in-house. 50 mg/kg of TEPP-46 dissolved in 40% 2-hydroxypropyl-β-cyclodextrin (HBCD) in PBS was injected intraperitoneally 24 hours and 3 hours prior to irradiation with 5 fractions of 2 Gy. Drug treatments occurred daily on a 5 days on/2 days off basis until the end of experiment. Tumor volume was calculated using the formula: (length x width^2)/2. All xenograft studies were approved by Institutional Animal Care and Use Committee. Once the tumor size reached criteria for euthanasia, tumors were collected for immunohistochemistry processing.

Intracranial tumor model

Survival studies: Male NSG mice were put under deep anesthesia with 2-3% isoflurane (Vetone) and positioned on a stereotactic device (David Kopf instrument; Stoelting, Quintessential Stereotaxic Injector). Ophthalmic ointment (Bausch and Lomb) was applied to both eyes of the mouse following anesthesia and 5 mg/kg Carprofen (Zoetis) was administered subcutaneously as painkiller prior to surgery, and daily for 2 days post-surgery. The head of the mouse was shaved and disinfected with povidone-iodine and 70% ethanol before incision was made along the midline (~1 cm). A 1 mm diameter hole was drilled in the skull above the right cerebral hemisphere at 0.5 mm anterior and 2.25 mm lateral to the bregma. A 10 µl syringe (Hamilton Syringe) was loaded with 5 µl of cell suspension (GBM374 or GBM217), the tip of the needle was inserted 3.5 mm from the surface of the brain, then retracted 0.5 mm before injecting 2 µl of cell suspension (250,000 cells) at a rate of 0.4 µl/min. Mice were then removed from the stereotactic device, and bone wax (CP Medical, Inc) was applied to seal the hole in the skull. Incision was closed with tissue adhesive (3M Vetbond), and topical 2% Lidocaine (Akorn) was applied at site of wound closure. Tumor burden was monitored through bioluminescence imaging (Ivis Lumina II, Perkin Elmer) before starting treatments. TEPP46 was dissolved in 40% HBCD and was administered intraperitoneally at 24 hours and 3 hours prior to irradiation with a single dose of 8 Gy, at the right cerebral hemisphere. Drug treatments occurred daily on a 5 days on/2 days off basis for 3 weeks. Mice were euthanized when they showed neurological symptoms.

IHC staining: Hematoxylin and eosin staining were performed on 4 µm slides of paraffin-embedded intracranial tumors by the Translational Pathology Core Laboratory (TPCL) of UCLA and images were acquired at 4x with a Keyence BZ-9000 microscope (Keyence Corporation of America, Itasca, IL).

***In vivo* stable isotope tracing:** For *in vivo* metabolomics experiments, all animal procedures were approved by the University Committee on Use and Care of Animals at the University of Michigan. GBM38 cells were injected into the cranium of female 6-week-old Rag1 KO mice at a depth of 3 mm at coordinates of 2 mm forward and 1 mm lateral from the bregma. Four weeks after implants, catheters were placed in the carotid artery and jugular vein of anesthetized GBM38 brain tumor-bearing mice. Five days later, mice were treated with brain-directed RT (0 Gy or 8 Gy), immediately followed by the start of intravenous infusions with uniformly labeled ^{13}C-glucose. Awake, active mice were infused for a total of 4 hours constituting a 3-minute bolus of 0.4 mg/kg

^{13}C-glucose followed by continuous infusions of 0.012 mg/g/min ^{13}C-glucose. Mice were then euthanized, and fluorescent (GFP^+) GBM tissue was rapidly harvested on dry ice and flash frozen within 1 minute of euthanasia. Metabolites were extracted by homogenizing tissues in cold (-80 °C) 80% methanol and clarified by centrifugation. Samples were dried by speedvac and submitted to the University of Michigan Metabolomics Core for LC-MS performed with an Agilent system consisting of an Infinity Lab II UHPLC coupled with a 6470 Triple Quad (QqQ) mass spectrometer (Agilent Technologies). Metabolites were identified by matching retention times and mass (±10 ppm) to authentic standards. Tissues from mice infused with solvent only were used as negative controls. Isotope peak areas were integrated using MassHunter Profinder 10.0 (Agilent Technologies). Fractional labeling (FL) was calculated with the following equation, where *i* is the isotopologues, *n* is the number of carbon atoms in a metabolite, and *m* is the relative fraction of the isotopologues.

$$FL = \frac{\sum_{i=0}^{n} im_i}{n}$$

***In vivo* micro-Positron Emission Tomography (PET)/micro-computed tomography (CT) imaging:** Male NSG mice were implanted subcutaneously with GBM374 gliomaspheres. Once the tumors were palpable, mice were anesthetized with 1.5% vaporized isoflurane, and injected with the [^{18}F]-FDG via tail vein. Following 1-hour unconscious uptake, mice underwent micro-PET imaging (15 min static data acquisition) immediately followed by microCT imaging using the Genisys8 PET/CT scanner (Sofie Biosciences). PET data was decay corrected, and attenuation correction was performed using the CT images. Co-registered PET/CT data were analyzed and quantified by drawing 3D regions of interest (ROI) using the AMIDE software.

Brain penetration of PKM2-activator:

Sample Preparation: Naïve NSG mice were treated with 50 mg/kg TEPP46. At specific timepoints, whole blood from mice was collected by retroorbital bleeding and centrifuged to isolate plasma. TEPP46 was isolated by liquid-liquid extraction from plasma: 50 µL plasma was added to 2 µL internal standard and 150 µL acetonitrile. Mouse brain tissue was washed with 2 mL cold PBS and homogenized using a tissue homogenizer with fresh 2 mL of cold PBS. TEPP46 was then isolated and reconstituted in a similar manner by liquid-liquid extraction: 100 µL brain homogenate was added to 2 µL internal standard and 300 µL acetonitrile. After vortex mixing, the samples were centrifuged. The supernatant was removed and evaporated by a rotary evaporator and reconstituted in 100 µL 50:50:0.1 water:acetonitrile:formic acid.

TEPP46 Detection: Chromatographic separations were performed on a 100 x 2.1 mm Phenomenex Kinetex C18 column (Kinetex) using the 1290 Infinity LC system (Agilent). The mobile phase was composed of solvent A: 0.1% formic acid in Milli-Q water, and B: 0.1% formic acid in acetonitrile. Analytes were eluted with a gradient of 5-99% B (1-20 min), 99% B (20-25 min), and then returned to 5% B for 5 min to re-equilibrate between injections. Injections of 20 µL into the chromatographic system were used with a solvent flow rate of 0.10 mL/min.

Mass spectrometry was performed on the 6460 triple quadrupole LC/MS system (Agilent). Ionization was achieved by using electrospray in the positive mode and data acquisition was made in multiple reactions monitoring (MRM) mode. Two MRM transitions were used for TEPP46: m/z 373→ 358 and 373→ 79 with fragmentor voltage of 125V, and collision energy of 12 and 25 eV,

respectively. Analyte signal was normalized to the internal standard and concentrations were determined by comparison to the calibration curve (0.5, 5, 50, 250, 500, 2000 nM). TEPP46 brain concentrations were adjusted by 1.4% of the mouse brain weight for the residual blood in the brain vasculature, as described by Dai et al[7].

Statistics:

Subcutaneous tumor model: In the subcutaneous model the primary objective was to compare the tumor growth at 7 time points, for a total of 35 tumors, implanted on 12 mice at 3 distinct tumor sites, left flank, right flank and back. The analysis included the four treatment regimens: vehicle, 5x2Gy, TEPP46 and TEPP46+5x2Gy. The unit of normalized tumor size, as the percentage of baseline tumor size at day 0, was used throughout analysis.

Analysis of Variance (ANOVA) was used to determine whether the tumor size at day 11 differs among treatment groups or not. When a significant difference is found via ANOVA, a post-hoc analysis of TukeyHSD test was used to identify the specific pair with tumor size differences. For simplicity, the assumption that unique tumors are independent samples, regardless of the host mice, was imposed within ANOVA and its post-hoc analysis.

Growth curve analysis was carried out for the comparison of subcutaneous tumor growth curve among the different treatment groups. The spaghetti plot with average trend, summarized via locally weighted regression (lowess) method by treatment group, provides the visualization of the overall growth trend of each treatment group. The tumor growth curve was analyzed via smoothing splines method with smoothness parameter set to be a moderate value of 0.5. The linear mixed-effects model (LMM) with random effect, as an approach to assess whether the time effect on tumor size differs among treatment groups or not, was applied with accommodating the within-subject correlation in our dataset. While the smoothing splines method, as a nonparametric approach, allows us to estimate maximum growth without being restricted to a specific model formula, LMM, for simplicity, assuming the linear relation between tumor size and time, assesses whether the time effect differs among treatment groups via the interaction term of time and treatment. Likelihood ratio test (LRT) was applied to assess the overall significance of the interaction term within LMM.

Intracranial model: With the particular interest of comparing the overall survival (OS) among five treatment regimes, received by a different cohort of 56 male mice, time-to-event analysis was performed. On univariate analysis, Kaplan-Meier estimator/curve by treatment regime was derived along with the log-rank test to assess whether difference in OS among treatment regimens exists or not. On multivariable analysis, the relation between time to death and treatment regime with vehicle+8Gy as reference level, adjusting for weight of mice, was evaluated via Cox proportional hazards (Cox PH) model. The proportional hazards assumption was examined via the diagnostic plot method. LRT was applied to assess the overall significance of the treatment regime as categorical variable within Cox PH model.

Significance level was set at 5% and all tests were two-sided. All analyses were conducted using R 3.6.0/R 4.1.1[8] (R Foundation for Statistical Computing) with packages *statmod*[9,10], *growthrates*[11], *ggplot2*[12], *lme4*[13], *lmerTest*[14], *survival*[15,16], and *survminer*[17].

Unless otherwise stated, statistical significance was determined by performing two-sided t tests and two-way ANOVAs using Prism v9.3.0. *p* values were considered significant below 0.05 (*,

$p<0.05$; **, $p<0.01$, ***, $p<0.001$, ****, $p<0.0001$). All experiments were independently repeated at least 3 times.

All schematics were created with Biorender.com.

References

1 Laks, D. R. *et al.* Large-scale assessment of the gliomasphere model system. *Neuro-oncology* **18**, 1367-1378, doi:10.1093/neuonc/now045 (2016).

2 Zhou, W. *et al.* Purine metabolism regulates DNA repair and therapy resistance in glioblastoma. *Nature communications* **11**, 3811, doi:10.1038/s41467-020-17512-x (2020).

3 Yazal, T. *et al.* Radiosensitizing Pancreatic Cancer via Effective Autophagy Inhibition. *Molecular Cancer Therapeutics*, doi:10.1158/1535-7163.Mct-20-1103 (2021).

4 Zhang, L. *et al.* PK-M2-mediated metabolic changes in breast cancer cells induced by ionizing radiation. *Breast cancer research and treatment* **178**, 75-86, doi:10.1007/s10549-019-05376-9 (2019).

5 Park, J. O. *et al.* Near-equilibrium glycolysis supports metabolic homeostasis and energy yield. *Nat Chem Biol* **15**, 1001-1008, doi:10.1038/s41589-019-0364-9 (2019).

6 Wang, Y., Parsons, L. R. & Su, X. AccuCor2: isotope natural abundance correction for dual-isotope tracer experiments. *Lab Invest* **101**, 1403-1410, doi:10.1038/s41374-021-00631-4 (2021).

7 Dai, H., Marbach, P., Lemaire, M., Hayes, M. & Elmquist, W. F. Distribution of STI-571 to the brain is limited by P-glycoprotein-mediated efflux. *J Pharmacol Exp Ther* **304**, 1085-1092, doi:10.1124/jpet.102.045260 (2003).

8 R: A language and environment for statistical computing. R Foundation for Statistical Computing. *http://www.R-project.org/* (2019/2021).

9 Baldwin, T. *et al.* Wound healing response is a major contributor to the severity of cutaneous leishmaniasis in the ear model of infection. *Parasite Immunol* **29**, 501-513, doi:10.1111/j.1365-3024.2007.00969.x (2007).

10 Elso, C. M. *et al.* Leishmaniasis host response loci (lmr1-3) modify disease severity through a Th1/Th2-independent pathway. *Genes Immun* **5**, 93-100, doi:10.1038/sj.gene.6364042 (2004).

11 Petzoldt, T. growthrates: Estimate Growth Rates from Experimental Data. R package version 0.8.2. *https://CRAN.R-project.org/package=growthrates* (2020).

12 Wickham, J. ggplot2: Elegant Graphics for Data Analysis. *Springer-Verlag New York* (2016).

13 Bates D, M., M.; Bolker, B.; Walker, S. Fitting Linear Mixed-Effects Models Using lme4. . *Journal of Statistical Software* **67**, 1-48. doi:10.18637/jss.v18067.i18601. (2015).

14 Kuznetsova, A. B., P.B.; Christensen, R.H.B. . lmerTest Package: Tests in Linear Mixed Effects Models. *Journal of Statistical Software* **82**, 1-26. doi: 10.18637/jss.v18082.i18613 (URL: https://doi.org/18610.18637/jss.v18082.i18613). (2017).

15 Terry, M. T. P. M. G. Modeling Survival Data: Extending the Cox Model. *Springer, New York* **ISBN 0-387-98784-3** (2000).

16 Therneau, T. A Package for Survival Analysis in R. R package version 3.2-11. *URL: https://CRAN.R-project.org/package=survival* (2021).

17 Kassambara, A. K., M.; Biecek, P. survminer: Drawing Survival Curves using 'ggplot2'. R package version 0.4.8. *https://CRAN.R-project* (2020).